Diffracted and pseudo-physical waves from spatially limited arrays using source–receiver interferometry (SRI)

Katrin Löer,[1] Giovanni Angelo Meles,[1] Andrew Curtis[1] and Ivan Vasconcelos[2]

[1] *Grant Institute of Earth Science, School of Geosciences, The University of Edinburgh, The King's Buildings, Edinburgh, EH9 3JW, UK.*
E-mail: katrin.loer@ed.ac.uk
[2] *Schlumberger Gould Research Centre, High Cross, Madingley Road, Cambridge, CB3 0EL, UK*

SUMMARY

Source–receiver interferometry (SRI) refers to a technique to construct the Green's function between a source and a receiver using only energy that has travelled from and to surrounding boundaries of sources and receivers. If a background medium is perturbed, the corresponding interferometric equation can be expressed as the sum of eight terms, which result from the separation of the total wavefield into an unperturbed background field and the perturbed scattered field. Here, the contribution of each individual term is identified for singly diffracted waves using the methods of stationary phase analysis and waveform modelling. When the data acquisition boundary requirements for seismic interferometry are violated, non-physical energy is introduced into Green's function estimates. Our results show that four terms produce purely non-physical, non-stationary energy and that these can be suppressed, and that a combination of only two terms can be used to estimate diffracted wavefields robustly. One of the two terms is precisely that used in geophysical imaging schemes. A key result is that this term also produces non-physical energy, except when the integration boundaries are truncated to span only part of the medium's free surface: we thus show that in this sense, partial boundaries can be seen as a positive advantage for migration or imaging methods. The other term produces non-physical energy which nevertheless emulates physical energy; such energy is therefore called *pseudo-physical*. We present for the first time a complete mathematical derivation of this new category of energy complemented with illustrative examples. Overall, this work significantly enhances our understanding of how scattered wave SRI works.

Key words: Interferometry; Theoretical seismology; Wave scattering and diffraction; Acoustic properties.

INTRODUCTION

Seismic or wavefield interferometry commonly refers to the use of wavefields from a boundary of sources recorded at two receivers to construct the signal that would have been obtained at one of the two receivers if the other receiver had instead been an impulsive source (Lobkis & Weaver 2001; Campillo & Paul 2003; Derode *et al.* 2003; Wapenaar 2004; van Manen *et al.* 2005, 2006; Wapenaar *et al.* 2005). This signal is referred to as the Green's function of the medium and is estimated by cross-correlation, convolution, or deconvolution of the wavefields measured at the two receiver positions. This technique is known as interreceiver interferometry since it yields the Green's function between two receivers, turning one receiver into a so-called 'virtual' (imagined) source. Further types of interferometry are referred to as either intersource (Hong & Menke 2006; Curtis *et al.* 2009) or source–receiver interferometry, also referred to as SRI (Curtis & Halliday 2010). These construct either the Green's function between two sources from the wavefield

recorded at an enclosing boundary of receivers, or the Green's function between a source and a receiver using only the energy that has propagated to surrounding receivers or from surrounding sources. Example canonical geometries for these three types of interferometry are shown in Fig. 1, and reviews and tutorials on the various methods are given in Curtis *et al.* (2006), Wapenaar *et al.* (2010a,b) and Galetti & Curtis (2012).

Recently, Halliday & Curtis (2010) derived an explicit link between scattered-wave SRI and seismic imaging or migration, a common technique used in exploration geophysics to map reflecting and diffracting discontinuities in the subsurface (Claerbout 1985; Oristaglio 1989). As has been shown by Halliday & Curtis (2010), Vasconcelos *et al.* (2010), and Ravasi & Curtis (2013), seismic interferometry has the potential to improve current migration schemes since it can circumvent the need for the single-scattering Born approximation and is in principle able to account for all possible nonlinearities, such as those due to multiply scattered waves. Other potential applications of SRI are ground-roll removal (Duguid
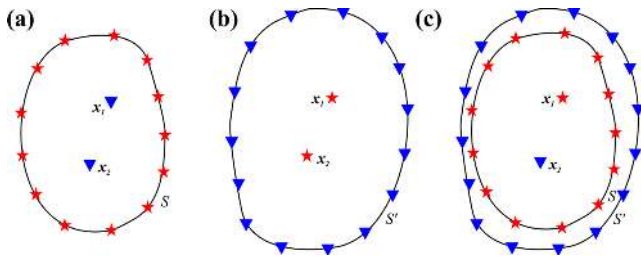
Figure 1. Three example canonical configurations used in wavefield interferometry to construct the Green's function between locations $\mathbf{x}_1$ and $\mathbf{x}_2$. Triangles indicate receivers, stars indicate sources, and S and S' denote a source and a receiver boundary, respectively. **(a)** Interreceiver interferometry: the receiver at either $\mathbf{x}_1$ or $\mathbf{x}_2$ is turned into a virtual source using the wavefields generated by the surrounding sources on S. **(b)** Intersource interferometry: the source at either $\mathbf{x}_1$ or $\mathbf{x}_2$ is turned into a virtual receiver using the wavefield response recorded on the receiver boundary S'. **(c)** Source–receiver interferometry (SRI): the Green's function between a real source and a real receiver can be constructed using the energy travelling from and to the surrounding boundaries S and S' of sources and receivers, respectively.

et al. 2011) or reflection imaging from below or above the reflector (Poliannikov 2011; Poliannikov *et al.* 2012).

Scattering occurs in all regimes of energy propagation (acoustic, elastic, electromagnetic, etc.) when the propagating wavefield interacts with perturbations inside the medium. In general, one distinguishes between reflected energy which originates from structures such as interstrata interfaces, and diffracted energy which originates from structures of small spatial extent compared to the wavelength, such as angular boundaries, voids, faults, or fractures. Although standard industrial seismic imaging procedures were originally developed based on diffracted energy (Miller *et al.* 1987), they are principally designed to image reflecting interfaces rather than diffracting structures. However, understanding and imaging diffractions is a topic of ongoing research (Khaidukov *et al.* 2004; Berkovitch *et al.* 2009; Faccipieri *et al.* 2013), as it helps to interpret recorded data and to enhance the resolution of seismic images. In this study, we use SRI to construct the diffracted wavefield associated with a single isotropic point diffractor, also referred to here as scatterer, in an otherwise homogeneous medium. The simplicity of this medium allows us to illuminate the internal workings of SRI for diffracted energy.

The principles of seismic interferometry can be illustrated using the method of stationary phase (see Appendix A). Although mainly applicable for relatively simple media it provides a means to understand the underlying physics and the generation of so-called spurious or non-physical energy in estimated Green's functions (Snieder *et al.* 2006, 2008; Halliday & Curtis 2009; Mikesell *et al.* 2009; King & Curtis 2012). Using stationary phase analysis, Snieder (2004a,b) showed that the main contribution to the constructed Green's function in coda-wave interferometry comes from so-called stationary points (Appendix A). Waves radiated from sources in regions near these points interfere constructively, whereas waves coming from sources in non-stationary regions destructively cancel each other when summing or integrating over a complete source boundary.

In theory, interferometry requires complete, closed boundaries of sources or receivers that surround a portion of the medium of interest. In practice, however, this can seldom be realized (for example, it is usually impossible to place a complete boundary of sources in the interior of solid bodies) so often only partial boundaries, usually spatially limited arrays on the Earth's surface, are available. In addition the spatial sampling density of sources or receivers along the surface may not fulfil the usual Nyquist requirements of wavefield

sampling. In such cases, spurious or non-physical energy appears in the interferometric results giving errors in the Green's function estimates due, for example, to incomplete destructive interference of energy from non-stationary regions or to the omission of sources or receivers at or around stationary points. These non-physical events are not per se unfavourable: it has been shown (Mikesell *et al.* 2009; King & Curtis 2011, 2012; King *et al.* 2011; Harmankaya *et al.* 2013; Meles & Curtis 2013) that non-physical energy can in fact be used to extract physical information about the medium. However, our ability to use such energy originates from our understanding of how it relates to physical properties and recording geometries.

In this work we contribute to a deeper understanding of SRI in a scattering medium. We expand the kinematic analysis of Meles & Curtis (2013) by considering also dynamic waveforms of events constructed from SRI, and analyse the effect of limited integration boundaries represented by linear source and receiver arrays on one side of the medium. We examine the origin of non-physical diffracted energy by invoking the method of stationary phase, and focus on a new category of non-physical energy which emulates physical energy and is therefore referred to as 'pseudo-physical'. We present a new mathematical derivation that explains the origin of pseudo-physical energy, and use a numerical model to demonstrate the construction of physical, non-physical, and pseudo-physical energy in the Green's function estimates. In the supporting information, we provide a detailed parametric study of each term of the interferometric equation in SRI, illustrating the sensitivity of different terms to changes in the model parameters and in the data processing, and showing how this can be used to suppress undesired non-physical and non-stationary arrivals. As a result, this paper shows how non-physical energy can be suppressed, how pseudo-physical energy is related to physical energy, and how all these types of energy can be used to interrogate the interior of a solid medium such as the Earth.

SOURCE–RECEIVER INTERFEROMETRY IN A SCATTERING MEDIUM

SRI constructs the signal between a source and a receiver using the energy travelling from and to surrounding boundaries of sources and receivers. It can be thought of as a combination of interreceiver and intersource interferometry, performed sequentially. In the following we focus on the specific geometry shown in Fig. 2, where the outer boundary, S, is the source boundary and the inner boundary, S', is a receiver boundary (these may be interchanged without loss of generality). The first step of SRI comprises the construction of the so-called homogeneous Green's functions $G_h(\mathbf{x}', \mathbf{x}_2) = G(\mathbf{x}', \mathbf{x}_2) + G^*(\mathbf{x}', \mathbf{x}_2)$ between the receiver at $\mathbf{x}_2$ and any receiver at $\mathbf{x}'$ on boundary S' using

$$G\left(\mathbf{x}', \mathbf{x}_2\right) + G^*\left(\mathbf{x}', \mathbf{x}_2\right) = \frac{-1}{j\omega\rho} \int_S \left\{ G(\mathbf{x}_2, \mathbf{x})\partial_i G^*(\mathbf{x}', \mathbf{x}) \right.$$

$$\left. - [\partial_i G(\mathbf{x}_2, \mathbf{x})]G^*(\mathbf{x}', \mathbf{x}) \right\} n_i \, \mathrm{d}S, \quad (1)$$

(Wapenaar & Fokkema 2006) where $j = \sqrt{-1}$, ω denotes the angular frequency, ρ denotes the density of the medium (assumed to be constant herein), $G(\mathbf{x}', \mathbf{x})$ is the Green's function between a source at $\mathbf{x}$ and a receiver at $\mathbf{x}'$, $n_i \partial_i G$ is a Green's function's derivative in direction i, the star * denotes complex conjugation, and the integration is over variable $\mathbf{x}$. The Einstein summation convention applies to repeated indices. Note that the explicit dependency on frequency in the
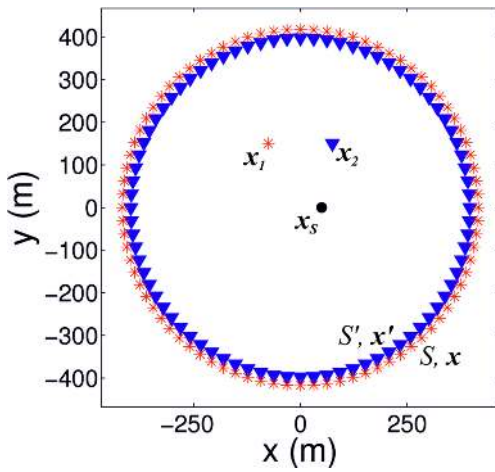
Figure 2. Geometry for source–receiver interferometry with complete boundaries. Stars are sources, triangles are receivers, and the black dot marks the location of an isotropic point scatterer. $\mathbf{x}$ denotes any source on source boundary S, $\mathbf{x}'$ denotes any receiver on receiver boundary S'.

Green's functions has been dropped for notational convenience only, and all expressions herein are in the frequency domain. For each receiver pair this is equivalent to standard interreceiver interferometry: the wavefields from each source on $\mathbf{x}$ recorded at one receiver pair at $\mathbf{x}'$ and $\mathbf{x}_2$ are cross-correlated and summed (integrated) over source positions. This turns one of the receivers, here the central receiver at $\mathbf{x}_2$, into a virtual source, as can be seen in terms $G(\mathbf{x}', \mathbf{x}_2)$ on the left-hand side. In the second step we construct the homogeneous Green's function $G_h(\mathbf{x}_2, \mathbf{x}_1) = G(\mathbf{x}_2, \mathbf{x}_1) + G^*(\mathbf{x}_2, \mathbf{x}_1)$ between the real source at $\mathbf{x}_1$ and the virtual source at $\mathbf{x}_2$, using the recorded wavefields between $\mathbf{x}_1$ and points on S', and the interreceiver wavefields between $\mathbf{x}_2$ and points on S' obtained in the first step. This corresponds to intersource interferometry and is given by

$$G(\mathbf{x}_2, \mathbf{x}_1) + G^*(\mathbf{x}_2, \mathbf{x}_1) = \frac{-1}{j\omega\rho} \int_{S'} \left\{ G^*(\mathbf{x}', \mathbf{x}_2) \partial_i' G(\mathbf{x}', \mathbf{x}_1) \right.$$
$$\left. - [\partial_i' G^*(\mathbf{x}', \mathbf{x}_2)] G(\mathbf{x}', \mathbf{x}_1) \right\} n_i' \mathrm{d}S' \quad (2)$$

(Hong & Menke 2006). The Green's function $G^*(\mathbf{x}', \mathbf{x}_2)$ required in eq. (2) can be obtained from the homogeneous Green's function $G_h(\mathbf{x}', \mathbf{x}_2)$ (eq. 1) by windowing the acausal part of the time-domain signal then transforming back to the frequency domain. Assuming that the Sommerfeld radiation conditions (Born & Wolf 1999) apply, we can write the Green's functions' derivatives in eqs (1) and (2) as $n_i \partial_i G = \mp j(\omega/c)G$, where c is velocity and '−' and '+' indicate outgoing or incoming waves, respectively (Wapenaar & Fokkema 2006). This reduces the integrals to the simpler forms

$$G(\mathbf{x}', \mathbf{x}_2) + G^*(\mathbf{x}', \mathbf{x}_2) \approx \frac{2}{\rho c} \int_S G(\mathbf{x}_2, \mathbf{x}) G^*(\mathbf{x}', \mathbf{x}) \, \mathrm{d}S, \quad (3)$$

$$G(\mathbf{x}_2, \mathbf{x}_1) + G^*(\mathbf{x}_2, \mathbf{x}_1) \approx \frac{2}{\rho c} \int_{S'} G^*(\mathbf{x}', \mathbf{x}_2) G(\mathbf{x}', \mathbf{x}_1) \, \mathrm{d}S' \quad (4)$$

(Curtis *et al.* 2012). We will refer to eqs (3) and (4) as the 'monopole approximation' because the dipole sources and receivers indicated by the Green's functions' derivatives in eqs (1) and (2), are approximated by monopole sources and receivers in eqs (3) and (4). Sommerfeld's radiation conditions assume that all ray paths are normal to the boundaries. Eqs (3) and (4) can be combined to a more

applicable form,

$$G(\mathbf{x}_2, \mathbf{x}_1) + G^*(\mathbf{x}_2, \mathbf{x}_1) \approx \frac{4}{(\rho c)^2} \iint_{S \, S'} G(\mathbf{x}', \mathbf{x}_1) G(\mathbf{x}_2, \mathbf{x})$$

$$\times \, G^*(\mathbf{x}', \mathbf{x}) \, \mathrm{d}S' \mathrm{d}S - \frac{2}{\rho c} \int_{S'} G(\mathbf{x}', \mathbf{x}_1) G(\mathbf{x}', \mathbf{x}_2) \, \mathrm{d}S' \quad (5)$$

$$\approx \frac{4}{(\rho c)^2} \iint_{S \, S'} G(\mathbf{x}', \mathbf{x}_1) G(\mathbf{x}_2, \mathbf{x}) G^*(\mathbf{x}', \mathbf{x}) \, \mathrm{d}S' \mathrm{d}S, \quad (6)$$

(Curtis & Halliday 2010), where the second integral in eq. (5) goes to zero if the radiation condition applies, that is, if the boundaries are in the far-field and are perpendicular to the out-going wavefield. This expression allows a clear understanding of the problem that is presented in the following.

As shown in Fig. 2 we assume a scattering medium and herein we consider only the case of a single scatterer or diffractor. In this case it is useful to separate the full wavefield G into the unperturbed background field G_0, which would be obtained if the scatterer was not present, and the perturbed or scattered field G_S defined according to

$$G = G_0 + G_S, \quad (7)$$

where G is any Green's function measured in the perturbed medium. Substituting eq. (7) for each Green's function in eq. (6) gives a double-surface integral over the sum of eight terms:

$$G(\mathbf{x}_2, \mathbf{x}_1) + G^*(\mathbf{x}_2, \mathbf{x}_1) = [G_0(\mathbf{x}_2, \mathbf{x}_1) + G_S(\mathbf{x}_2, \mathbf{x}_1)]$$
$$+ \, [G_0(\mathbf{x}_2, \mathbf{x}_1) + G_S(\mathbf{x}_2, \mathbf{x}_1)]^*$$
$$\approx \frac{4}{(\rho c)^2} \iint_{S \, S'} [G_0(\mathbf{x}', \mathbf{x}_1) G_0(\mathbf{x}_2, \mathbf{x}) G_S^*(\mathbf{x}', \mathbf{x})$$
$$+ \, G_S(\mathbf{x}', \mathbf{x}_1) G_S(\mathbf{x}_2, \mathbf{x}) G_S^*(\mathbf{x}', \mathbf{x})$$
$$+ \, G_0(\mathbf{x}', \mathbf{x}_1) G_S(\mathbf{x}_2, \mathbf{x}) G_S^*(\mathbf{x}', \mathbf{x})$$
$$+ \, G_S(\mathbf{x}', \mathbf{x}_1) G_0(\mathbf{x}_2, \mathbf{x}) G_S^*(\mathbf{x}', \mathbf{x})$$
$$+ \, G_0(\mathbf{x}', \mathbf{x}_1) G_0(\mathbf{x}_2, \mathbf{x}) G_0^*(\mathbf{x}', \mathbf{x})$$
$$+ \, G_S(\mathbf{x}', \mathbf{x}_1) G_S(\mathbf{x}_2, \mathbf{x}) G_0^*(\mathbf{x}', \mathbf{x})$$
$$+ \, G_0(\mathbf{x}', \mathbf{x}_1) G_S(\mathbf{x}_2, \mathbf{x}) G_0^*(\mathbf{x}', \mathbf{x})$$
$$+ \, G_S(\mathbf{x}', \mathbf{x}_1) G_0(\mathbf{x}_2, \mathbf{x}) G_0^*(\mathbf{x}', \mathbf{x})] \, \mathrm{d}S' \mathrm{d}S, \quad (8)$$

where subscript 0 refers to a direct wave and subscript S refers to a scattered wave (Vasconcelos *et al.* 2009). A similar decomposition is presented by Vasconcelos (2013), which includes all of the gradient terms at both source and receiver locations similarly to eqs (1) and (2), rather than invoking the monopole approximation in eqs (3) and (4) as above.

The double integral on the right-hand side of eq. (8) can be evaluated using stationary phase analysis. This method has been used in standard interferometry (Snieder *et al.* 2006, 2008; Halliday & Curtis 2009; Snieder & Fleury 2010) to analyse interferometric integrals assuming that the main contribution to the integrand comes from so-called stationary points (Appendix A). Recently, Meles & Curtis (2013) have performed stationary phase analysis for the kinematics of SRI. Due to the double boundary the stationary points of interreceiver interferometry become stationary point-pairs (or just

Table 1. Stationary point pairs for different terms in eq. (8) (see Fig. 3; Meles & Curtis 2013). **x** refers to a source and **x′** to a receiver location. The events constructed occur at traveltimes associated with the causal direct wave (blue), the acausal direct wave (blue, underlined), the causal scattered wave (green), and the acausal scattered wave (green, underlined). Events constructed from stationary points marked red do not relate to physical arrivals.

| Terms in the integrand of eq. (8)	Corresponding stationary pairs	
$G_0(x', x_1)G_0(x_2, x)G_0^*(x', x)$	$\mathbf{x = a, x' = b};$	$\underline{\mathbf{x = b, x' = a}}$
$G_0(x', x_1)G_S(x_2, x)G_0^*(x', x)$	$\mathbf{x = e, x' = f};$	$\mathbf{x = f, x' = e}$
$G_S(x', x_1)G_0(x_2, x)G_0^*(x', x)$	$\mathbf{x = d, x' = c};$	$\mathbf{x = c, x' = d}$
$G_S(x', x_1)G_S(x_2, x)G_0^*(x', x)$	**Any pair connected by a straight line passing through the scatterer**	
$G_0(x', x_1)G_0(x_2, x)G_S^*(x', x)$	$\underline{\mathbf{x = e, x' = c}};$ $\underline{\mathbf{x = f, x' = d}};$	$\mathbf{x = d, x' = e}$ $\mathbf{x = c, x' = f}$
$G_0(x', x_1)G_S(x_2, x)G_S^*(x', x)$	$\forall\mathbf{x = x, x' = f};$	$\forall\mathbf{x, x' = e}$
$G_S(x', x_1)G_0(x_2, x)G_S^*(x', x)$	$\mathbf{x = d, \forall x'};$	$\mathbf{x = c, \forall x'}$
$G_S(x', x_1)G_S(x_2, x)G_S^*(x', x)$	**Any pair**	
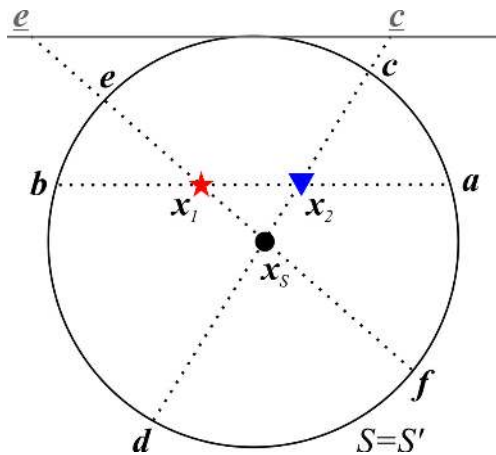
Figure 3. Stationary points (**a** to **f**) for source–receiver interferometry in a homogeneous medium containing a single point scatterer. Symbol key as in Fig. 2. The source and receiver boundary coincide and are represented by the circular solid line. A stationary pair consists of a boundary source and receiver at a pair of stationary points. The combination of stationary points in this pair varies for each term. Points <u>e</u> and <u>c</u> are projections of points **e** and **c** on to a horizontal surface (such as the Earth's surface in seismic interferometry in a vertical plane).

pairs) consisting of a stationary point **x** on source boundary *S* and a stationary point **x′** on receiver boundary *S′* (Table 1, Fig. 3). We invoke this method of analysis below and in the supporting information.

NON-PHYSICAL AND PSEUDO-PHYSICAL ENERGY

An event constructed from interferometry is referred to as 'non-physical' if it does not correspond to a physical wave that would propagate between the source and receiver locations $\mathbf{x}_1$ and $\mathbf{x}_2$, such as a direct or scattered wave. Fig. 4(a) illustrates geometrically how one such event is generated as an example. Snieder *et al.* (2008) analysed the properties of non-physical events in interreceiver interferometry in a scattering medium. They showed the contributions from different terms (in their case four terms rather than eight) towards physical and non-physical energy, and how non-physical
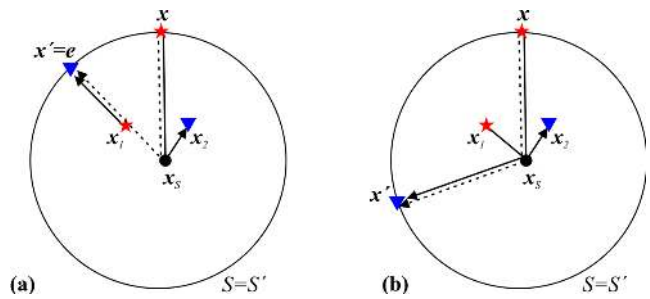
Figure 4. Generation of non-physical and pseudo-physical energy from different terms in eq. (8) and Table 1; symbol key as in Fig. 2. Solid ray paths indicate traveltimes that are added to the phase of the result of eq. (8), the dashed line indicates a traveltime that is subtracted from the phase: hence, portions of solid and dashed lines that span the same path give phase contributions that exactly cancel. **(a)** $G_0 G_S G_S^*$: the stationary point **e** on *S′* and any point **x** on *S* give rise to a stationary, but non-physical event with a traveltime equal to $t(\mathbf{x}_2, \mathbf{x_S}) - t(\mathbf{x}_1, \mathbf{x_S})$, where $t(\mathbf{x}_2, \mathbf{x}_s)$ is the traveltime from point $\mathbf{x}_s$ to $\mathbf{x}_2$. **(b)** $G_S G_S G_S^*$: any source–receiver pair on the boundary is stationary and gives rise to a non-physical event with a traveltime equal to that of the physical diffracted wave. The kinematics of this energy thus emulates that of physical energy, and hence, the event is called 'pseudo-physical'.

energy is cancelled out after the summation of all terms and integration over a closed boundary. If, however, the different terms of the integrand are used separately, or if the boundary is not complete, the non-physical energy does not cancel out but instead gives spurious contributions to the interferometric estimate.

Geophysical seismic imaging as well requires integration over boundaries. It is well known that artefacts in the image occur due to limited boundaries: sources and receivers can usually only be placed on the Earth's surface and hence cannot be said to surround any portion of the medium through which the energy propagates and which we hope to image (the subsurface). From interferometry we now understand that these artefacts correspond to non-physical energy that is not cancelled out due to missing sources and receivers in the subsurface.

In SRI, unlike in standard interferometry, we find that some non-physical energy arrives at exactly the traveltime of the expected scattered waves, thus approximately (or exactly) emulating physical energy. Fig. 4(b) illustrates how such a pseudo-physical event is constructed from SRI when using diffracted waves G_S only, that is, within the term $G_S G_S G_S^*$. For this term, any source–receiver pair on the boundaries is stationary and is sufficient to construct the event (Meles & Curtis 2013; Fig. 3 and Table 1). This property makes the term $G_S G_S G_S^*$ particularly useful when boundaries are only partially available or are strongly decimated, as is often the case in practical experiments. Note that the stationarity properties of this term only apply to diffracted waves; for reflecting media the behaviour is substantially different. As has been shown by Meles & Curtis (2013), the traveltime of the constructed event equals the traveltime of the causal scattered wave. They point out, however, that the interferometric event is only *proportional* to the causal scattered wave: its amplitude also depends on a real factor λ. Expanding their analysis, we provide in the following a detailed mathematical derivation explaining the origin of pseudo-physical energy in SRI and the properties of λ for 2-D and 3-D Green's functions. The derivation below is complemented by an alternative derivation based on the scattered wave representation theorems of Vasconcelos *et al.* (2009) given in Appendix B.

We start by rewriting the diffracted wavefield as a concatenation of direct waves according to

$$G_S\left(\mathbf{x}_2, \mathbf{x}_1\right) = G_0\left(\mathbf{x}_S, \mathbf{x}_1\right) A\left(\mathbf{k}_2, -\mathbf{k}_1\right) \tilde{G}_0\left(\mathbf{x}_2, \mathbf{x}_S\right), \qquad (9)$$

(Snieder *et al.* 2008; Wapenaar *et al.* 2010c) where $\mathbf{x}_S$ is the location of a point scatterer, $A\left(\mathbf{k}_2, -\mathbf{k}_1\right)$ is the complex-valued scattering matrix, $-\mathbf{k}_1$ is the direction of the incident wavefield, and $\mathbf{k}_2$ the direction of the scattered wavefield. In the far field, the Green's function $G_0\left(\mathbf{x}_S, \mathbf{x}_1\right)$ in 2-D is defined as

$$G_0\left(\mathbf{x}_S, \mathbf{x}_1\right) = -\frac{\rho\omega}{4} \mathrm{e}^{-i(k|\mathbf{x}_S - \mathbf{x}_1|)} \sqrt{\frac{2}{\pi k\, |\mathbf{x}_S - \mathbf{x}_1|}}, \qquad (10)$$

and the volume injection Green's function $\tilde{G}_0\left(\mathbf{x}_2, \mathbf{x}_S\right)$ is given by

$$\tilde{G}_0\left(\mathbf{x}_2, \mathbf{x}_S\right) = \frac{1}{\rho\omega} G_0\left(\mathbf{x}_2, \mathbf{x}_S\right) = -\frac{1}{4} \mathrm{e}^{-i(k|\mathbf{x}_2 - \mathbf{x}_S|)} \sqrt{\frac{2}{\pi k\, |\mathbf{x}_2 - \mathbf{x}_S|}}. \qquad (11)$$

For isotropic point scatterers the scattering matrix $A\left(\mathbf{k}_2, -\mathbf{k}_1\right)$ in eq. (9) does not depend on the direction of the incident wavefield, and an equal amount of energy is scattered in any direction; hence the scattering matrix can be abbreviated as a scalar A. Substituting eq. (9) for each Green's function in $G_S G_S G_S^*$, rearranging the terms, and using eqs (10) and (11) gives

$$\frac{4}{(\rho c)^2} \iint\limits_{S\ S'} G_S\left(\mathbf{x}', \mathbf{x}_1\right) G_S\left(\mathbf{x}_2, \mathbf{x}\right) G_S^*\left(\mathbf{x}', \mathbf{x}\right) \mathrm{d}S' \mathrm{d}S$$

$$= G_0\left(\mathbf{x}_2, \mathbf{x}_S\right) A \tilde{G}_0\left(\mathbf{x}_S, \mathbf{x}_1\right)$$

$$\times A A^* \frac{4}{(\rho c)^2} \int\limits_S G_0\left(\mathbf{x}_S, \mathbf{x}\right) G_0^*\left(\mathbf{x}_S, \mathbf{x}\right) dS$$

$$\times \int\limits_{S'} \tilde{G}_0\left(\mathbf{x}', \mathbf{x}_S\right) \tilde{G}_0^*\left(\mathbf{x}', \mathbf{x}_S\right) \mathrm{d}S'$$

$$= G_S\left(\mathbf{x}_2, \mathbf{x}_1\right) \times A A^* \frac{1}{16\pi} \int\limits_S \frac{1}{|\mathbf{x}_S - \mathbf{x}|} dS \int\limits_{S'} \frac{1}{|\mathbf{x}' - \mathbf{x}_S|} \mathrm{d}S'. \quad (12)$$

Without loss of generality we assume that the scatterer is located at the origin $\mathbf{x}_S = [0, 0]$, so that the terms in the integrands simplify to $1/|\mathbf{x}|$ and $1/|\mathbf{x}'|$, respectively. In the case of circular boundaries it is convenient to move to a polar coordinate system, such that $|\mathbf{x}| = r$, $|\mathbf{x}'| = r'$, $\mathrm{d}S = r\mathrm{d}\phi$, and $\mathrm{d}S' = r'\mathrm{d}\phi'$. Integration over ϕ and ϕ' from 0 to 2π shows that each surface integral reduces to a factor 2π (note that when the boundaries are only partially available each surface integral in eq. (9) will give a fraction of 2π depending on the portion of the circle included in the boundaries). From the relationship between real and imaginary parts of the scattering amplitude (optical theorem) it follows that $A A^* = -4\Im(A)$, with $0 \geq \Im(A) \geq -4$, where $\Im(A)$ is the imaginary part of A (Groenenboom & Snieder 1995; Snieder 1999; Galetti *et al.* 2013). Consequently, eq. (12) becomes

$$\frac{4}{(\rho c)^2} \iint\limits_{S\ S'} G_S\left(\mathbf{x}', \mathbf{x}_1\right) G_S\left(\mathbf{x}_2, \mathbf{x}\right) G_S^*\left(\mathbf{x}', \mathbf{x}\right) \mathrm{d}S' \mathrm{d}S$$

$$= G_S\left(\mathbf{x}_2, \mathbf{x}_1\right) \times [-\Im(A)]. \qquad (13)$$

Eq. (13) shows that the contribution of the term $G_S G_S G_S^*$ from complete boundaries equals the causal scattered wave $G_S\left(\mathbf{x}_2, \mathbf{x}_1\right)$ multiplied by a real-valued positive constant that is proportional to
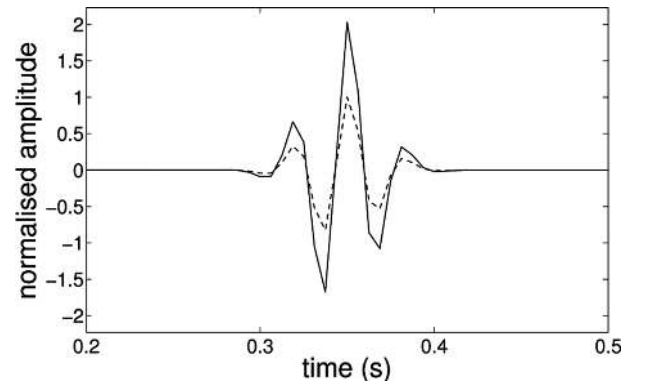
Figure 5. Interferometric result of the cross-term $G_S G_S G_S^*$ in eq. (8) (solid line) compared to the modelled causal scattered wave $G_S(\mathbf{x}_2, \mathbf{x}_1)$ (dashed line) using 2-D Green's functions and complete circular boundaries. Amplitudes have been normalized with respect to the maximum of the modelled trace. The imaginary part of the scattering matrix A has been set to -2; hence, according to eq. (13), the interferometric result equals $2G_S(\mathbf{x}_2, \mathbf{x}_1)$.

the imaginary part of the scattering matrix. This causes an amplitude change but no shift in phase or traveltime compared to the modelled arrival $G_S\left(\mathbf{x}_2, \mathbf{x}_1\right)$ (Fig. 5). For partial boundaries the overall amplitude is reduced according to the portion of the circle included in the boundaries. Thus we show that although the term $G_S G_S G_S^*$ is non-physical, in 2-D it provides the correct traveltime and waveform of the causal scattered wave, hence, it is *pseudo*-physical. If the scatterer is non-isotropic the scattering matrix $A\left(\mathbf{k}_2, -\mathbf{k}_1\right)$ cannot be reduced to the scalar A and the analysis is more complicated. The amplitude of the pseudo-physical arrival will then be a function of the source and receiver positions relative to the scatterer. Nevertheless, the kinematic analysis applies just as well for non-isotropic scatterers, which allows us to estimate the traveltime of the causal scattered wave.

The above results are only valid for the 2-D case where the 2-D Green's functions defined in eqs (10) and (11) are used. Using 3-D Green's functions and the corresponding relationship $A A^* = -\frac{4\pi}{k}\Im(A)$ (see Galetti *et al.* 2013), eq. (13) changes to

$$\frac{4}{(\rho c)^2} \iint\limits_{S\ S'} G_S\left(\mathbf{x}', \mathbf{x}_1\right) G_S\left(\mathbf{x}_2, \mathbf{x}\right) G_S^*\left(\mathbf{x}', \mathbf{x}\right) \mathrm{d}S' \mathrm{d}S$$

$$= G_S\left(\mathbf{x}_2, \mathbf{x}_1\right) \times (-k\pi)\Im(A). \qquad (14)$$

Since $k = \frac{\omega}{c}$ the result now depends on the frequency content and therefore distorts the waveform (Fig. 6a). However, this effect can be removed by dividing the result by k (in the frequency domain), and thus the correct traveltime and waveform information can also be obtained from the contribution of $G_S G_S G_S^*$ in the 3-D case (Fig. 6b).

Note that the non-physical energy provided by $G_S G_S G_S^*$ would be destructively cancelled out within an integration over complete boundaries that included the summation over all terms in eq. (8). Destructive cancellation occurs on account of other terms that provide non-physical energy at the same traveltime but with opposite phase. Following similar arguments as for $G_S G_S G_S^*$, it can be shown that this cancelling energy is provided by the terms $G_0 G_0 G_S^*$, $G_0 G_S G_0^*$, $G_0 G_S G_S^*$, $G_S G_0 G_S^*$, and $G_S G_S G_0^*$ (*cf.* Table 1). Thus we can also show that only the term $G_S G_0 G_0^*$ constructs the physical causal scattered wave (*cf.* eqs (B1) and (B2)), given that the integration boundaries span the stationary point pair associated with that term ($\mathbf{x} = \mathbf{d}$, $\mathbf{x}' = \mathbf{c}$ in Fig. 3).
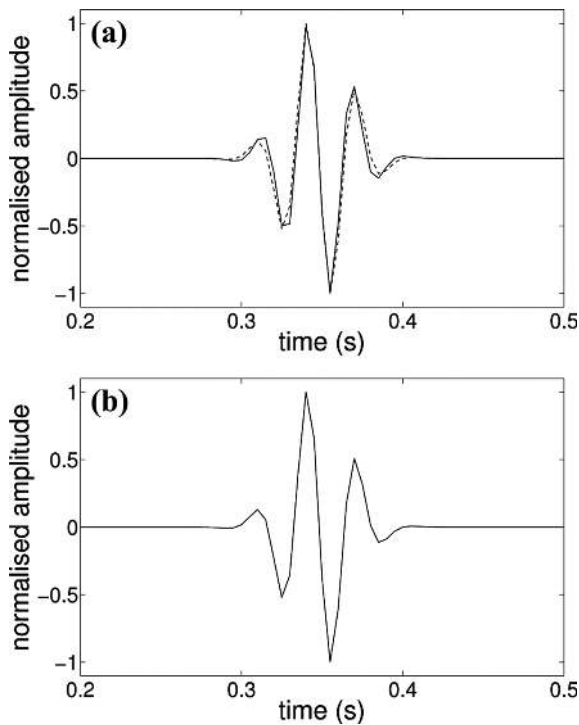
Figure 6. (a) Interferometric result of the term $G_S G_S G_S^*$ in eq. (8) (solid line) compared to the modelled causal scattered wave $G_S(\mathbf{x}_2, \mathbf{x}_1)$ (dashed line) using 3-D Green's functions and the geometry shown in Fig. 7. Amplitudes have been normalized with respect to the maximum of each trace. (b) As in (a) but divided by the wavenumber k in the frequency domain (*cf.* eq. (14)): the waveforms of the two curves are now identical.

NUMERICAL EXAMPLES

In the numerical examples that follow, the integration boundaries S and S' are reduced to finite linear arrays above the scatterer, as illustrated in Fig. 7. Compared to the ideal geometry in Figs 2 and 3, this omits some of the stationary points: in fact, only two stationary points **e̲** and **c̲**, equivalent to **e** and **c** (Table 1, Fig. 3), are populated by sources and receivers. To model acoustic wavefields in a scattering medium we use a direct scattering matrix-based scheme that is a variant of Foldy's method (Foldy 1945; Groenenboom & Snieder 1995; Galetti *et al.* 2013). This method yields the full, non-linear scattering response of multiple isotropic point scatterers embedded in an otherwise homogeneous medium. In the modelling code of Galetti *et al.* (2013), interreceiver and intersource interferometry are performed sequentially using eqs (3) and (4) for the full wavefield (monopoles and dipoles), or eqs (5) and (6) for the monopole approximation. The background velocity and density of the model
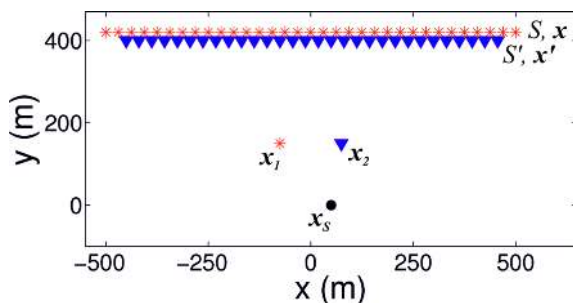
Figure 7. Geometry used for numerical examples with incomplete boundaries represented by linear source and receiver arrays; symbol key as in Fig. 2. Only every fifth source and receiver is plotted for clarity.

are here taken to be $v = 1000 \text{ m s}^{-1}$ and $\rho = 1 \text{ g cm}^{-3}$, respectively. The scatterer at $\mathbf{x}_S = [50, 0]$ is a point diffractor, the imaginary part of the scattering amplitude is chosen to be -2 in accordance with the conditions of the acoustic optical theorem (Groenenboom & Snieder 1995). The maximum frequency is $f_{\max} = 80 \text{ Hz}$ and the central frequency of the applied Ricker wavelet is $f_c = 30 \text{ Hz}$. The spatial sampling, that is, the intersource and interreceiver distance within the arrays, is controlled by the Nyquist wavelength λ_{Nyq} and is given by multiples of this value. λ_{Nyq} describes half the minimum wavelength defined by the velocity v and the temporal Nyquist frquency f_{Nyq} as

$$\lambda_{\text{Nyq}} = \frac{v}{f_{\text{Nyq}}} = \frac{v}{2 f_{\max}} = 6.25 \text{ m}, \tag{15}$$

given the signal's maximum frequency $f_{\max}$. The length of the source array is set to 1000 m and the receiver array is 900 m long, which gives a maximum of 161 sources and 144 receivers, respectively. The receiver array is located 20 m below the source array and 400 m above the diffractor. The single source is located at $\mathbf{x}_1 = [-75, 150]$ and the receiver at $\mathbf{x}_2 = [75, 150]$. The interferometric results are studied in the time domain in a window between –0.8 and 0.8 s. Negative times are referred to as the acausal part (in the frequency domain, the complex conjugate) of the Green's function and positive times represent the causal part.

In the examples shown in Figs 8 and 9 a spatial tapering function has been applied to the cross-correlated traces prior to the summation over sources and receivers. This means that the contributions associated with sources or receivers towards the endpoints of the arrays have been down weighted using half-cosine windowing functions.

The solid trace in Fig. 8 gives the interferometric estimate of the Green's function between $\mathbf{x}_1$ and $\mathbf{x}_2$ using the geometry in Fig. 7 and the full wavefield (i.e. all of eq. 8, but with incomplete integration boundaries) and the dashed trace represents the true Green's function modelled directly between $\mathbf{x}_1$ and $\mathbf{x}_2$. Table 2 provides the key to symbols used to denote parameter constellations employed in Fig. 8 and other figures. Since amplitudes of the constructed trace are expected to be incorrect due to the limited number of sources and receivers along the boundaries, the maximum amplitude of each trace has been normalized to one. Note that the normalization does not change the phase or the waveform shapes and therefore does not affect our analysis. Despite the incomplete boundaries, it appears
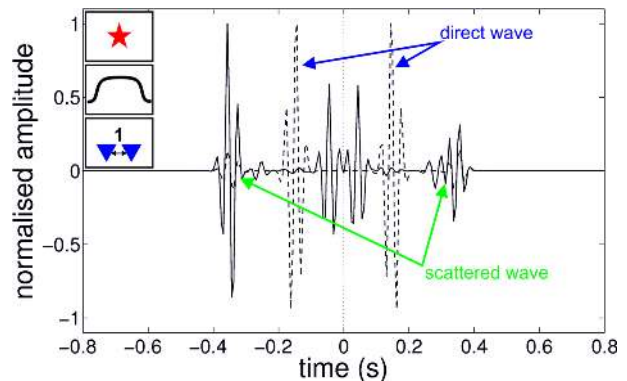
Figure 8. Source–receiver interferometric estimate of the Green's function between $\mathbf{x}_1$ and $\mathbf{x}_2$ using the full wavefield and the incomplete boundaries in Fig. 7 (solid line), compared to the true Green's function (dashed line). Amplitudes of each waveform have normalized maximum values. For legend key see Table 2.
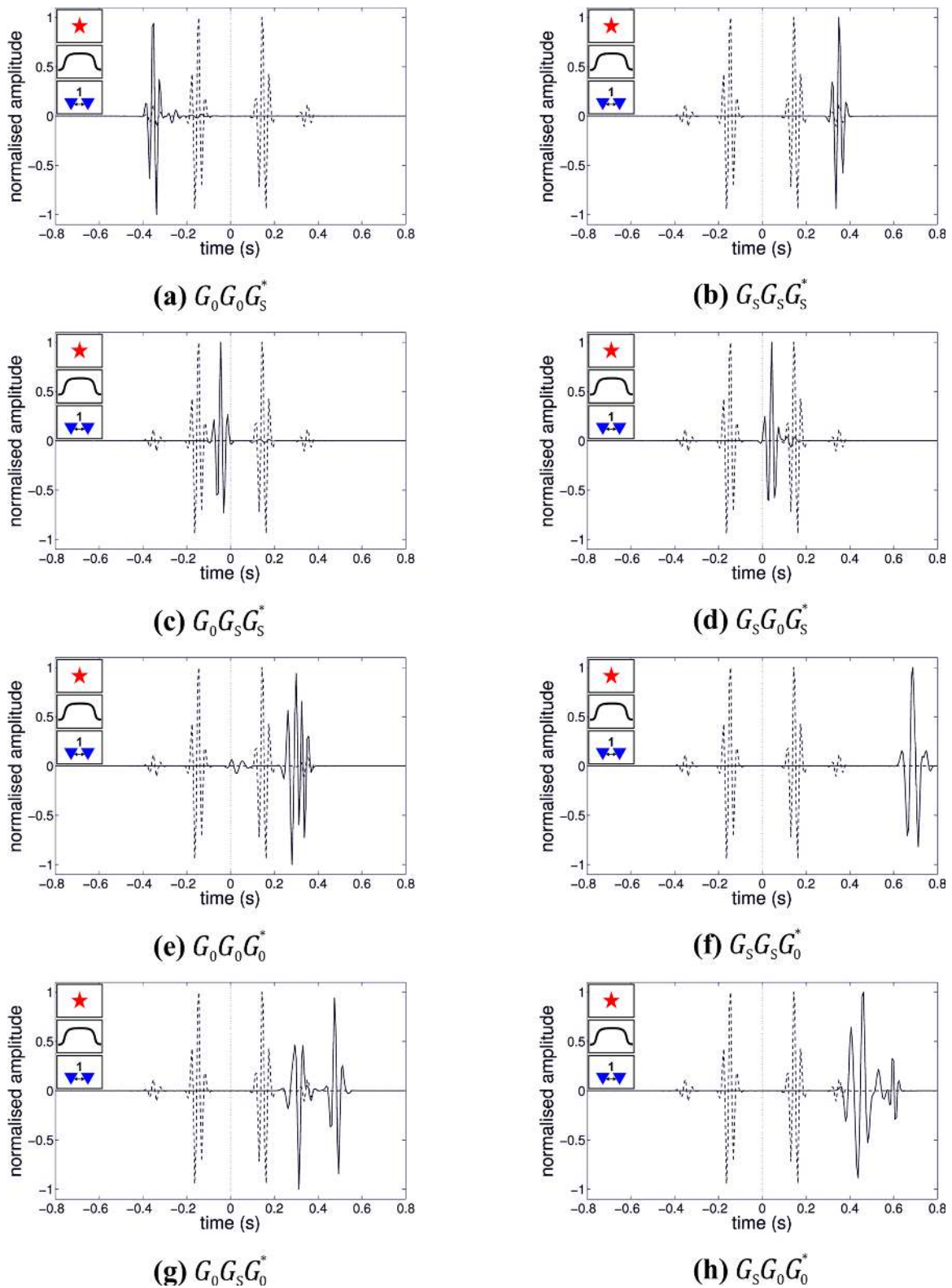
Figure 9. Interferometric result of integrating each term in eq. (8) separately (solid lines) compared to the true Green's function between $\mathbf{x}_1$ and $\mathbf{x}_2$ (dashed line). The term used in each case is noted beneath the plot. Model and processing parameters are defined according to the key symbols (Table 2). All maximum amplitudes have been normalized to one.

that both the causal and the acausal scattered wave are constructed surprisingly well from SRI. What is not apparent, however, is that the arrival that looks like the causal scattered wave is in fact a non-physical arrival, which has a physical traveltime, hence, is a pseudo-physical arrival. Moreover, note that non-physical events appear with differing amplitudes between zero time and the scattered wave arrivals for both positive and negative times. The direct wave is not recovered at all.

Table 2. Key to symbols used to denote parameter constellations employed in each numerical example. λ_{Nyq} indicates the spatial wavelength of the Nyquist frequency of the wavefield.
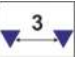
★	Only monopole sources/receivers are used on the boundary
★	Monopole and dipole sources/receivers are used on the boundary
⌒	A spatial half-cosine tapering weight is applied to the integrand towards the ends of the boundaries
⌀	No spatial half-cosine tapering weight is applied
▼1▼	The distance between two sources/receivers on a boundary equals $1 * \lambda_{\text{Nyq}}$
▼3▼	The distance between two sources/receivers on a boundary equals $3 * \lambda_{\text{Nyq}}$

Fig. 9 displays the contribution of each individual term (solid lines) of eq. (8), compared to the true Green's function between $\mathbf{x}_1$ and $\mathbf{x}_2$ (dashed line). The acausal scattered wave is solely constructed by the term $G_0 G_0 G_S^*$ (Fig. 9a) and the term $G_S G_S G_S^*$ contributes the above mentioned pseudo-physical arrival at the traveltime of the causal scattered wave (Fig. 9b). As has been demonstrated in the previous section, the pseudo-physical energy associated with the term $G_S G_S G_S^*$ can be used to estimate the waveforms of arriving physical energy.

All other terms generate events that cannot be associated with the expected Green's function and therefore count as non-physical events. The maximum amplitude in each trace has again been normalized to one; this means that the spurious events from the endpoints of the boundaries have been magnified in Figs 9(e)–(h) due to the normalization since they are the largest events on the trace. In fact, they have very low amplitudes—for example, the event in Fig. 9(f) does not show up at all in Fig. 8 because its amplitude is too small to see compared to the maximum amplitude in the full trace. In the supporting information we show systematically how different events are effected by variations in the model parameters, and by variations in the data processing.

To determine the origin of the constructed signals it is useful to display the so-called correlation gathers (van Manen *et al.* 2005; Mehta *et al.* 2008). In standard interreceiver interferometry the correlation gather is simply the set of integrands that are integrated in the interferometric equation. It provides the contribution of each source on the boundary to the interferometric estimate between two receivers, prior to the summation over sources. Zero-slope areas (i.e. flat areas) in the correlation gather indicate stationary points: the stationary phase approach assumes that the contributions from the Fresnel zone around such points sum constructively, while the contributions from all other source locations cancel each other out. In intersource interferometry the correlation gather displays the contribution for each specific receiver location. In source–receiver interferometry, however, we must consider both one correlation gather for each receiver pair in the first step (interreceiver interferometry), and the correlation gather of the (virtual) source pair in the second step (intersource interferometry).

In Fig. 10 we show the correlation gather of one specific receiver pair, namely the receiver at $\mathbf{x}_2$ and the leftmost receiver on boundary S' (location $\mathbf{x}_i'$), and the resulting correlation gather of the sources (one virtual, one real) located at $\mathbf{x}_1$ and $\mathbf{x}_2$ for each individual term. Some of the intersource correlation gathers exhibit zero traces ('gaps') over a range of receiver locations (e.g. Fig. 10j). These gaps occur when the interreceiver energy constructed in the first step (eq. 3) has positive arrival times only. According to eq. (2) only the acausal component $G^*(\mathbf{x}', \mathbf{x}_2)$, which corresponds to negative traveltimes, should be used in the second step. If this is zero, the cross-correlation $G^*(\mathbf{x}', \mathbf{x}_2) G(\mathbf{x}', \mathbf{x}_1)$ (see eq. 4) yields a zero trace and thus a gap in the correlation gather.

The correlation gathers reveal that the events—both physical and non-physical—constructed from the terms $G_0 G_0 G_S^*$, $G_S G_S G_S^*$, $G_0 G_S G_S^*$, and $G_S G_0 G_S^*$ (Figs 8a–h) originate from stationary points. Non-stationary contributions from the endpoints of the arrays are down-weighted by a cosine taper. The events constructed from $G_0 G_0 G_0^*$, $G_S G_S G_0^*$, $G_0 G_S G_0^*$, and $G_S G_0 G_0^*$ (Figs 8i–p) are non-physical and non-stationary without exception as they all originate from the endpoints of the arrays. As before, the traces related to the endpoint sources and receivers, respectively, are down weighted by a taper, however here the summed traces have been normalized to one, which especially magnifies these non-physical, non-stationary events.

DISCUSSION

In interferometry, using incomplete boundaries of sources and receivers, such as linear arrays, causes non-physical arrivals in Green's function estimates (Fig. 8) due to both inadequate sampling of stationary points and abrupt truncation of the boundaries. In the supporting information, we analyse the origin of physical, non-physical and pseudo-physical energy from each term in eq. (8) in detail. In this discussion we draw together the principal findings from above and from this supporting information.

We first distinguish between stationary and non-stationary non-physical events. Non-stationary events are associated with the contributions from sources and receivers at the endpoints of the arrays. They occur in every term, except for $G_S G_S G_S^*$ where every source–receiver pair is stationary and gives a pseudo-physical contribution (Appendix B; also Meles & Curtis 2013). As has been demonstrated in previous papers (e.g. Snieder *et al.* 2006) and throughout this study, the amplitudes of such non-stationary events can all be suppressed by down-weighting the contributions from the endpoints of surface arrays with a taper.

We also find that non-physical energy associated with the direct wave (non-scattered) Green's function $G_0^*(\mathbf{x}', \mathbf{x})$ can be reduced in amplitude by using the exact interferometric representation (eqs 1 and 2) rather than the monopole approximation (eqs 3 and 4). This is because $G_0^*(\mathbf{x}', \mathbf{x})$ does not fulfil the far-field assumptions when
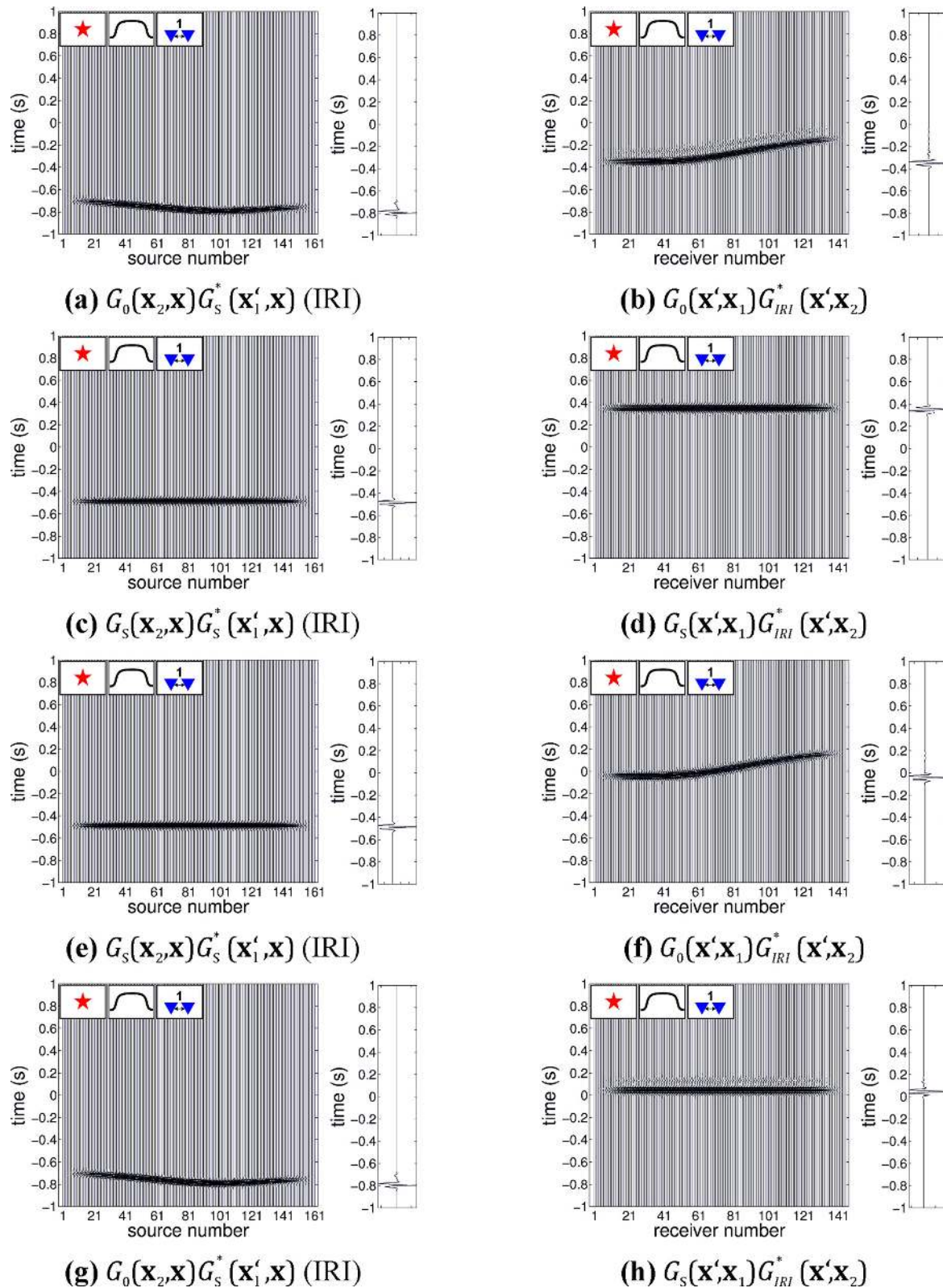
Figure 10. Correlation gathers for each term of eq. (8). The left-hand column displays the interreceiver interferometry results between the receiver at $\mathbf{x}_2$ and the leftmost receiver $\mathbf{x}'_l$ on boundary S' for each source on boundary S; the right-hand plot in the left-hand column gives the sum over all sources. The acausal part of this trace $G^*_{IRI}(\mathbf{x}'_l, \mathbf{x}_2)$ is then cross-correlated with $G_S(\mathbf{x}'_l, \mathbf{x}_1)$, which gives the leftmost trace in the gather in the right-hand column. The right-hand column displays the intersource interferometry results between the source at $\mathbf{x}_1$ and the virtual source at $\mathbf{x}_2$ for each receiver on boundary S'; the right-hand plot in the right-hand column gives the sum over all receivers showing how results in Fig. 9 are constructed. $G^*_{IRI}(\mathbf{x}', \mathbf{x}_2)$ refers to the result of interreceiver interferometry (IRI) carried out in the first step.
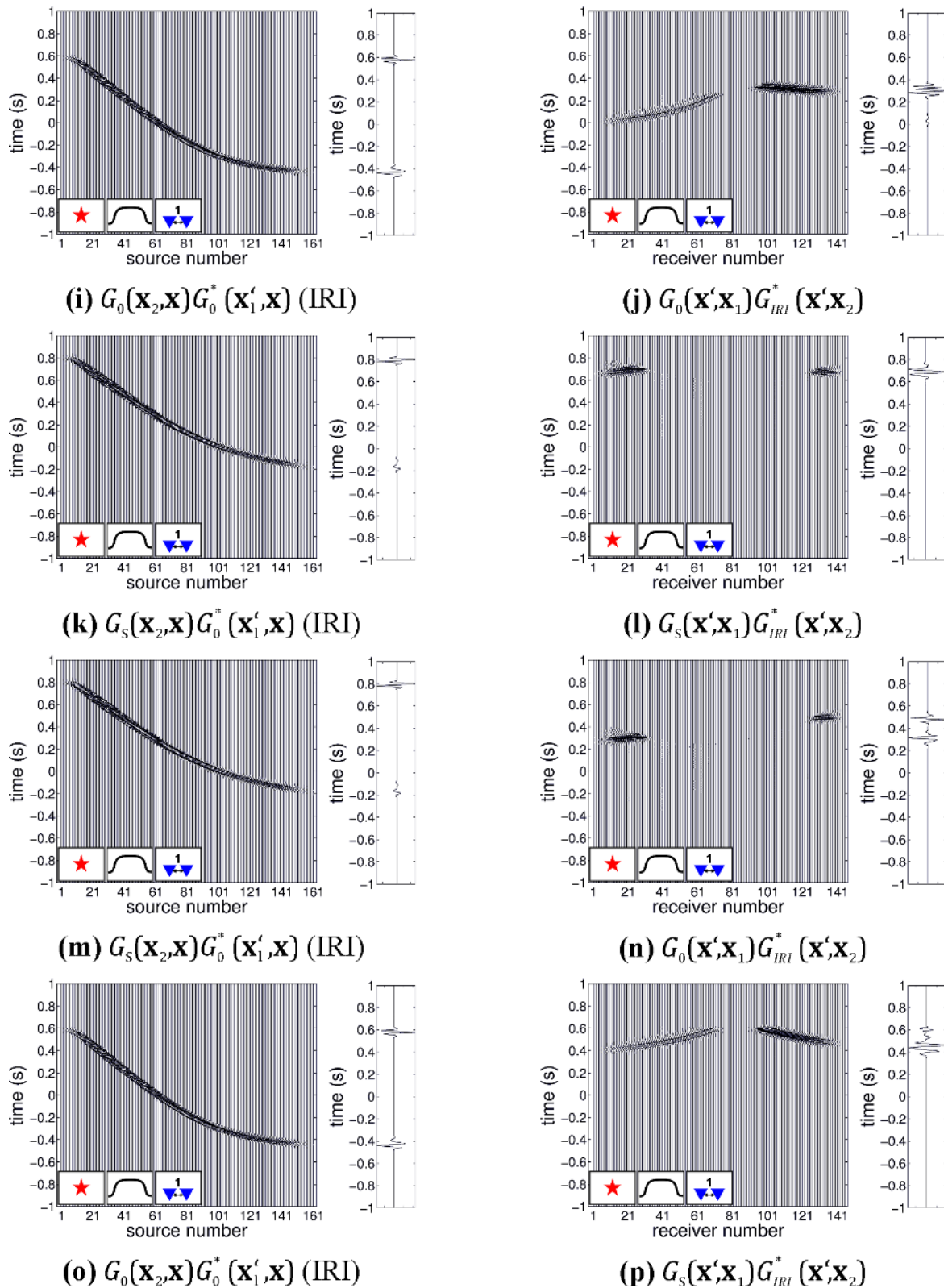
(i) $G_0(\mathbf{x}_2,\mathbf{x})G_0^*(\mathbf{x}_1',\mathbf{x})$ (IRI)

(j) $G_0(\mathbf{x}',\mathbf{x}_1)G_{IRI}^*(\mathbf{x}',\mathbf{x}_2)$

(k) $G_S(\mathbf{x}_2,\mathbf{x})G_0^*(\mathbf{x}_1',\mathbf{x})$ (IRI)

(l) $G_S(\mathbf{x}',\mathbf{x}_1)G_{IRI}^*(\mathbf{x}',\mathbf{x}_2)$

(m) $G_S(\mathbf{x}_2,\mathbf{x})G_0^*(\mathbf{x}_1',\mathbf{x})$ (IRI)

(n) $G_0(\mathbf{x}',\mathbf{x}_1)G_{IRI}^*(\mathbf{x}',\mathbf{x}_2)$

(o) $G_0(\mathbf{x}_2,\mathbf{x})G_0^*(\mathbf{x}_1',\mathbf{x})$ (IRI)

(p) $G_S(\mathbf{x}',\mathbf{x}_1)G_{IRI}^*(\mathbf{x}',\mathbf{x}_2)$

Figure 10 (*Continued.*)

boundaries S and S' are close to one-another (Fig. 7): the assumption that all ray paths (including those between the source and receiver boundaries) are normal to the boundaries is not valid in this case. (Note that when using $G_S^*(\mathbf{x}', \mathbf{x})$ instead of $G_0^*(\mathbf{x}', \mathbf{x})$, the assumption is more reasonable because the energy generated at the source

boundary travels towards the scatterer first before being recorded at the receiver boundary: provided the boundaries are far from the scatterer this leads to an ultimate propagation direction that is closer to the normal to the boundary.) In fact, terms $G_0G_0G_0^*$, $G_SG_SG_0^*$, $G_0G_SG_0^*$ and $G_SG_0G_0^*$ only contribute non-physical non-stationary
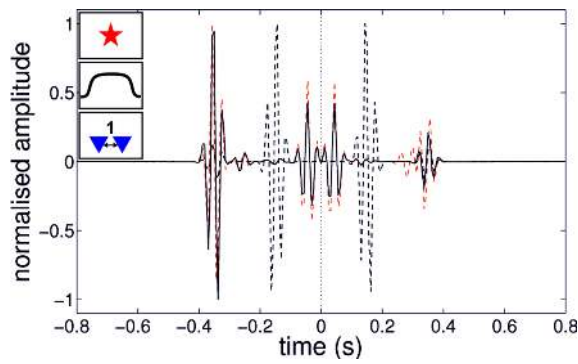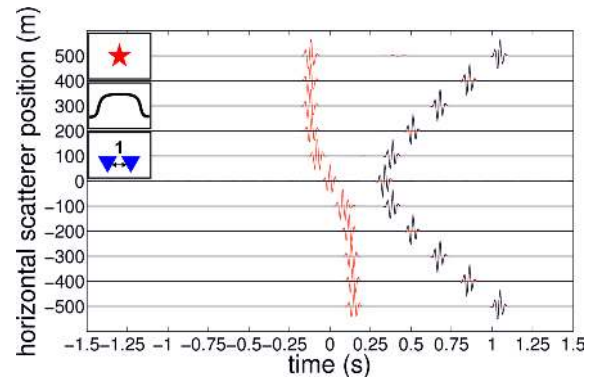
Figure 11. Source–receiver estimate of the Green's function between $\mathbf{x}_1$ and $\mathbf{x}_2$ (solid line) constructed using the partial boundaries in Fig. 7, when $G_0^*\left(\mathbf{x}', \mathbf{x}\right)$ is eliminated from the data prior to the cross-correlation. The dashed black line represents the true Green's function; the dashed red line corresponds to the interferometric trace in Fig. 8. Maximum amplitudes in each trace are normalized to one. The non-physical arrival before the pseudo-physical causal scattered wave in Fig. 8 is completely suppressed, resulting in a good estimate of the scattered wavefield.

Figure 12. Pseudo-physical (black lines) and non-physical (red lines) events constructed from $G_S G_S G_S^*$ and $G_0 G_S G_S^*$, respectively, for different horizontal scatterer positions—moving the scatterer in Fig. 7 relative to $\mathbf{x}_1$ and $\mathbf{x}_2$, while keeping the vertical location at 0 m. For any fixed scatterer position relative to $\mathbf{x}_1$ and $\mathbf{x}_2$ the position of the scatterer can be estimated using the combined traveltime information from both events.

energy. Since all of these terms, and only these terms, contain the direct wave arrival $G_0^*(\mathbf{x}', \mathbf{x})$ between boundaries S and S', eliminating this direct wave component altogether from the interferometry (i.e. setting it to zero prior to cross-correlating wavefields) reduces the amount of non-physical energy without losing physical information about the scattered wavefield (Fig. 11). In this way, the monopole or far-field approximation can be used without causing significant negative effects, even if the boundaries are close together or even if they are collocated.

Stationary but non-physical events are constructed from the terms $G_0 G_S G_S^*$ and $G_S G_0 G_S^*$ on account of the stationary pairs $\mathbf{x}' = \underline{\mathbf{c}}, \forall \mathbf{x}$ and $\mathbf{x} = \underline{\mathbf{e}}, \forall \mathbf{x}'$ (Fig. 3). Usually these events would be cancelled out by other non-physical events associated with the stationary points at $\mathbf{d}$ and $\mathbf{f}$. Using only partial boundaries, however, the linear arrays omit the corresponding stationary points and thus preserve the non-physical energy in the constructed trace. They are identified as the first arrivals, with traveltimes corresponding to $t(\mathbf{x}_2, \mathbf{x}_S) - t(\mathbf{x}_1, \mathbf{x}_S)$ and $t(\mathbf{x}_1, \mathbf{x}_S) - t(\mathbf{x}_2, \mathbf{x}_S)$, respectively, where $t(\mathbf{x}_1, \mathbf{x}_S)$ is the traveltime from $\mathbf{x}_S$ to $\mathbf{x}_1$. Although their traveltimes do not relate to physical ray paths they still contain information about the medium, especially about the location of the scatterer. For example, if the scatterer was located at the midpoint between source and receiver the traveltimes of both events would be zero and they would coincide at zero lag-time. We can thus use the information from the traveltimes of non-physical events to constrain the position of the scatterer. Combining this information with the traveltime of a physical scattered wave, causal or acausal, given by $t(\mathbf{x}_S, \mathbf{x}_1) + t(\mathbf{x}_2, \mathbf{x}_S)$ or $-[t(\mathbf{x}_S, \mathbf{x}_1) + t(\mathbf{x}_2, \mathbf{x}_S)]$, respectively, the position of a scatterer located below the source–receiver pair is uniquely defined (Fig. 12). Non-physical energy from standard interferometry has been well studied and shown to be useful in velocity analysis (King & Curtis 2011) and locating near-surface scatterers (Harmankaya *et al.* 2013). Similar applications appear feasible for non-physical energy constructed from SRI. Further research could examine the potential of using non-physical energy to constrain the scattering amplitude.

In the supporting information, we provide an analysis of different parametrizations of the numerical model using, for example, a larger spatial sampling interval while the lateral extents of S and S' are held constant. When the sampling interval is increased the contributions from neighbouring traces at non-stationary points may not cancel out and may thus introduce non-physical energy (see

Figs 13 and 14). Analysing each term of eq. (8) individually we find that some terms contribute energy that is relatively robust to changes of the sampling interval: the terms $G_0 G_0 G_S^*$ and $G_S G_S G_S^*$ still provide good estimates of the acausal and causal scattered wave, respectively, when the sampling interval equals six times the spatial Nyquist wavelength λ_{Nyq} (Fig. 15), which corresponds to a spacing of 38 m. This is also true for the stationary non-physical events in $G_0 G_S G_S^*$ and $G_S G_0 G_S^*$. Thus, the additional non-physical energy introduced by depopulating the boundaries appears solely on account of the terms $G_0 G_0 G_0^*$, $G_S G_S G_0^*$, $G_0 G_S G_0^*$ and $G_S G_0 G_0^*$, all of which contain the direct wave arrival between the two boundaries, $G_0(\mathbf{x}', \mathbf{x})$. Again, by eliminating this component prior to the cross-correlation of wavefields we can therefore reduce the amount of non-physical energy and apply a coarser source and receiver spacing without loss of resolution of the scattered waves.

The differing behaviour with respect to the spacing on each boundary can be understood by considering the correlation gathers: for each term, the maximum allowable spacing is determined by the slope of the traveltime curve in the correlation gather, which depends on the choice of the Green's functions in the cross-correlation. When $G_0(\mathbf{x}', \mathbf{x})$ is used rather than $G_S(\mathbf{x}', \mathbf{x})$ the traveltime curve in the first correlation gather (corresponding to interreceiver interferometry) has a much steeper slope (compare Figs 13 and 14, for example) and therefore causes incomplete cancellations even for a small increase of the sampling interval above the Nyquist wavelength. In general, the traveltime slope depends on the velocity of the medium, the depth of the source–receiver pair, and the depth of the scatterer (Mehta *et al.* 2008). Further, the behaviour of the traveltime curves may be different for multiply scattered or reflected waves. The maximum allowable spacing is thus defined by the geometry and material properties of the problem at hand.

For the geometry used, only the term $G_0 G_0 G_S^*$ gives the acausal scattered wave (Figs 9a, 10a and b) on account of the stationary pair $\mathbf{x} = \underline{\mathbf{e}}, \mathbf{x}' = \underline{\mathbf{c}}$ (Fig. 3). This term has also been used by Poliannikov (2011) to recover the reflection response of a layered medium using SRI. Moreover, an estimate of the causal scattered wave is obtained from the pseudo-physical event constructed from $G_S G_S G_S^*$ (Fig. 9b), for which every source-receiver pair is stationary (Figs 10c and d). Note that in the geometry used herein, $G_S G_S G_S^*$ is the only term that contains information about the causal scattered wave. If we therefore use only terms $G_0 G_0 G_S^*$ and $G_S G_S G_S^*$, we obtain a good estimate of the causal and acausal scattered field (Figs 15a
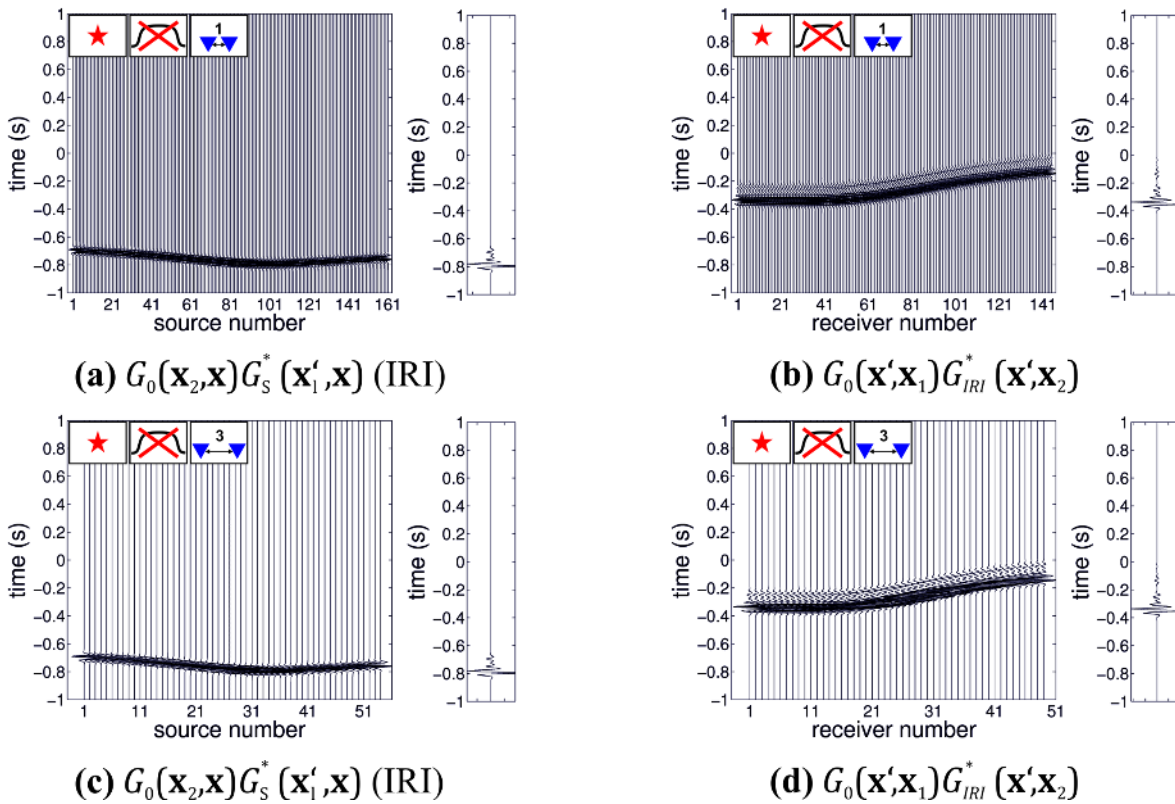
Figure 13. Correlation gathers of $G_0 G_0 G_S^*$ for different parameter constellations (for symbol key see Table 2). Panels (a) and (b) correspond to (a) and (b) in Fig. 10. (c) As in (a) but with the source interval equal to $3 * \lambda_{Nyq}$. (d) As in (b) but with the receiver interval equal to $3 * \lambda_{Nyq}$. Figure layout as in Fig. 10. In this example the coarser spatial sampling does not affect the interferometric result.
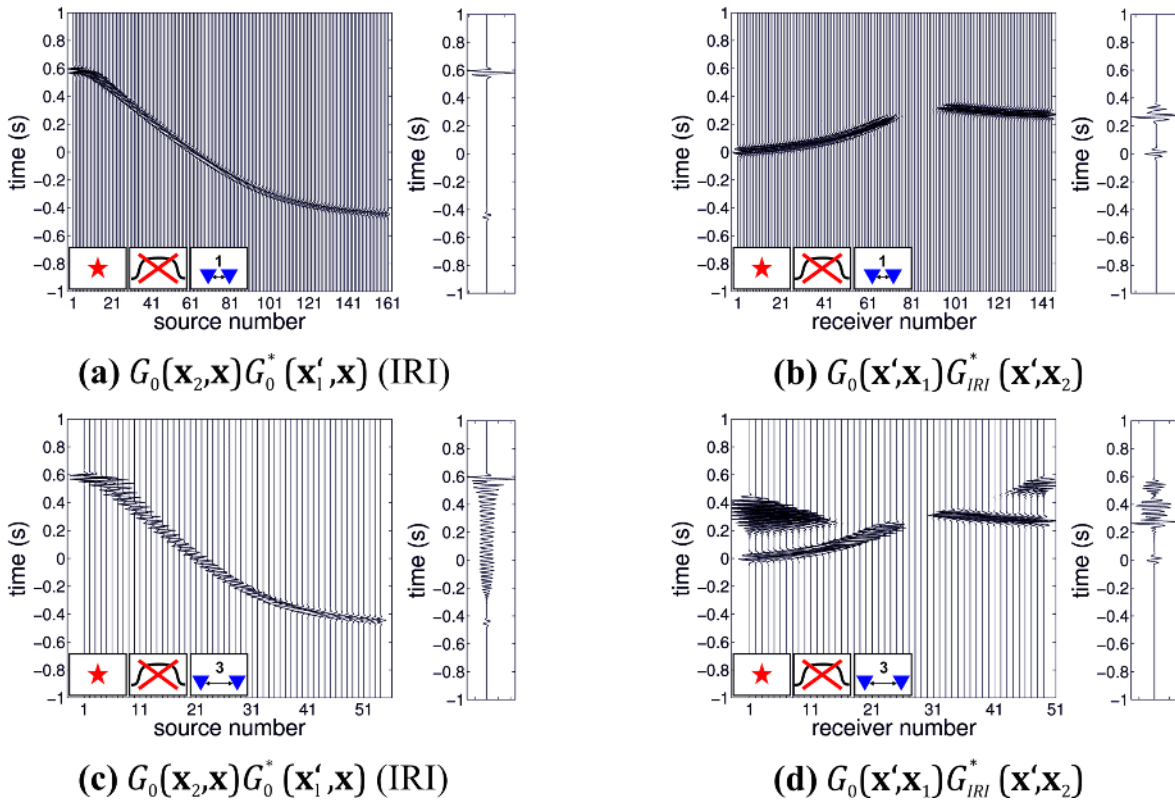
Figure 14. As in Fig. 13 but for $G_0 G_0 G_0^*$. (a) and (b) above correspond to (i) and (j) in Fig. 10. When a coarser spatial sampling is applied (c and d) additional non-physical energy is introduced in the interferometric estimate.

(a) $G_0 G_0 G_S^* + G_S G_S G_S^*$

(b) $G_0 G_0 G_S^* + G_S G_S G_S^*$

(c) $G_0 G_0 G_S^* + G_S G_S G_S^*$
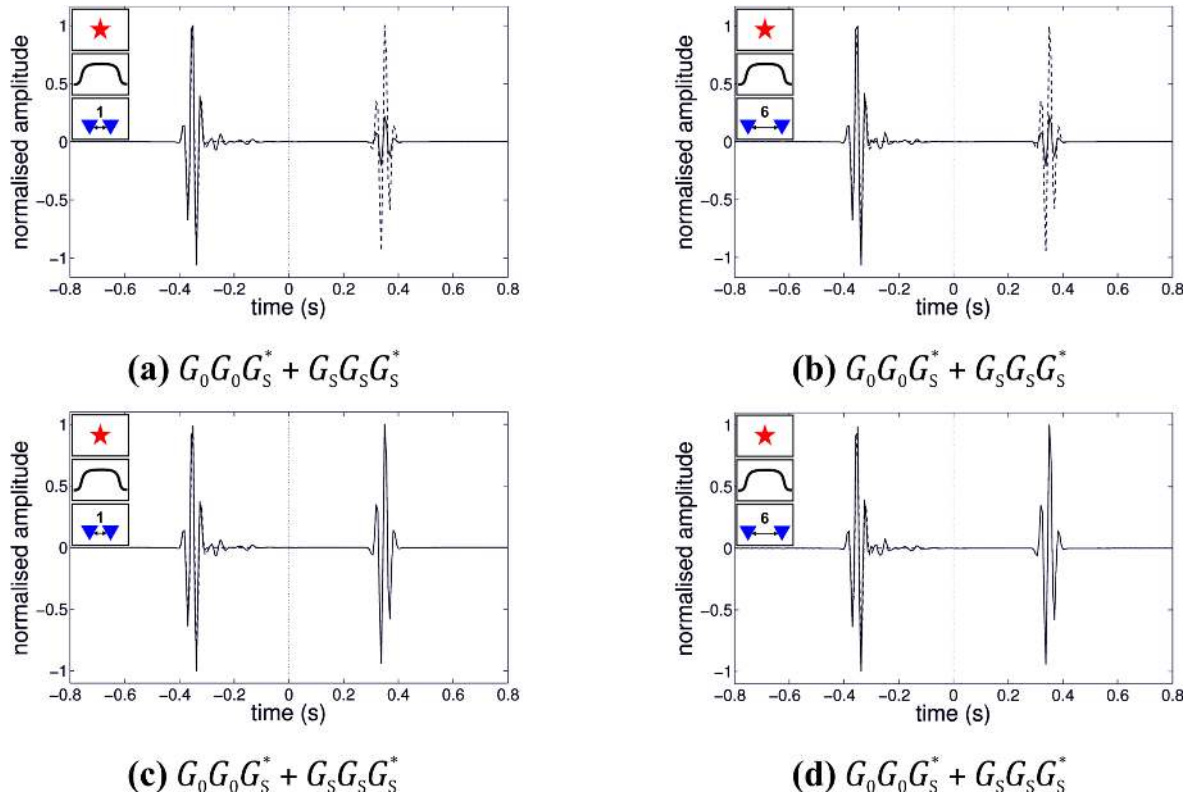
(d) $G_0 G_0 G_S^* + G_S G_S G_S^*$

Figure 15. (Pseudo-)Physical scattered wave energy constructed using the terms $G_0 G_0 G_S^*$ and $G_S G_S G_S^*$ only (solid line) compared to the true scattered wave (dashed line). The maximum amplitudes have been normalized to one. (a) Source and receiver spacing is equal to $1 * \lambda_{\text{Nyq}}$. (b) Source and receiver spacing is equal to $6 * \lambda_{\text{Nyq}}$. (c) and (d) show the same results as (a) and (b), but causal and acausal (positive and negative time) sides have been normalized independently to better illustrate the quality of the interferometric result. Despite the strongly depleted boundaries in (b) and (d) the scattered wavefield is well constructed and no additional spurious energy is introduced.

and c) even if the boundary source and receiver sampling is depleted (Figs 15b and d).

Considering the applicability of these results in an imaging context, when the aim is to image the scatterer we have to consider the following limitations: compared to the geometry used in SRI (Fig. 7), in a seismic experiment the subsurface source at $\mathbf{x}_1$ and the receiver at $\mathbf{x}_2$ are physically not available, so the wavefields $G(\mathbf{x}', \mathbf{x}_1)$ and $G(\mathbf{x}_2, \mathbf{x})$ are not recorded. In imaging methods these wavefields are modelled using a smooth background model, usually obtained from velocity analysis and waveform inversion (Pratt 1999; Yilmaz 2001). Under these conditions we find that $G_0 G_0 G_S^*$ has a crucial advantage over $G_S G_S G_S^*$: while modelling of $G_S(\mathbf{x}', \mathbf{x}_1)$ and $G_S(\mathbf{x}_2, \mathbf{x})$ requires information about the scatterer (which is usually not available from the background model), $G_0(\mathbf{x}', \mathbf{x}_1)$ and $G_0(\mathbf{x}_2, \mathbf{x})$ are solely defined by the background model. In fact, $G_0 G_0 G_S^*$ can be compared directly to the imaging condition for a migrated image (Claerbout 1985) given that source and receiver coincide on the image point $\mathbf{x}_1$, since the explicit link between imaging and SRI was provided by Halliday & Curtis (2010). They derive the scattered wave components of SRI from reciprocity relations for perturbed media, and show that under the Born approximation the scattering potential f at a point $\mathbf{x}_1$ is given by

$$f(\mathbf{x}_1) = \frac{-4}{j c_0} \int_{-\infty}^{\infty} d\omega (-j\omega) \times \int_{S} \left[\partial_i \Phi(\mathbf{x}_1, \mathbf{x}) G_0^*(\mathbf{x}_1, \mathbf{x}) \right.$$
$$\left. - \Phi(\mathbf{x}_1, \mathbf{x}) \partial_i G_0^*(\mathbf{x}_1, \mathbf{x}) \right] n_i dS, \tag{16}$$

where $\Phi(\mathbf{x}_1, \mathbf{x})$ represents the back propagated wavefield at $\mathbf{x}_1$

$$\Phi(\mathbf{x}_1, \mathbf{x}) = \frac{-1}{j \omega \rho} \int_{S'} \left[\partial_{i'} G_S(\mathbf{x}', \mathbf{x}) G_0^*(\mathbf{x}_1, \mathbf{x}') \right.$$
$$\left. - G_S(\mathbf{x}', \mathbf{x}) \partial_{i'} G_0^*(\mathbf{x}_1, \mathbf{x}') \right] n_{i'} dS'. \tag{17}$$

Note that $G_0(\mathbf{x}_1, \mathbf{x})$ and $G_0(\mathbf{x}_1, \mathbf{x}')$ are not measured quantities but synthetic forward-propagating (from sources at $\mathbf{x}$) and back-propagating (from receivers at $\mathbf{x}'$) Green's functions, respectively, calculated using the background model. As Halliday & Curtis (2010) explain, eq. (16) is directly related to the imaging condition that Oristaglio (1989) derived using a double-focussing algorithm. We find that eqs (16) and (17) show striking similarities to eqs (2) and (1), respectively, assuming that $\mathbf{x}_2 = \mathbf{x}_1$, and setting $G(\mathbf{x}', \mathbf{x}_1) = G_0(\mathbf{x}', \mathbf{x}_1)$, $G(\mathbf{x}_2, \mathbf{x}) = G_0(\mathbf{x}_2, \mathbf{x})$, as if using the term $G_0 G_0 G_S^*$ only and invoking source–receiver reciprocity.
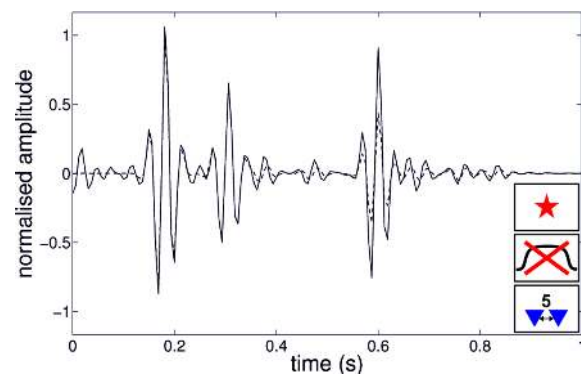
Note that Halliday & Curtis (2010) use a complete circular boundary of sources and receivers. In their derivation they find that not only the zero-offset scattering response is constructed but also its time reverse, as well as two events similar to stationary but non-physical arrivals in interferometry. This is consistent with the events expected from the term $G_0 G_0 G_S^*$ by stationary phase analysis when using a full boundary (Table 1). When restricting the boundary to the surface, however, only the acausal scattered wave is constructed due to the lack of stationary points associated with the causal scattered wave and the two stationary, non-physical events. Hence an
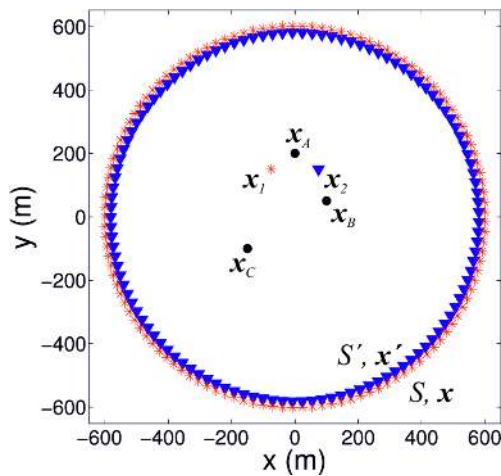
Figure 16. Geometry used in multiple diffractors example. Symbol key as in Fig. 2. The imaginary part of the scattering amplitude of the diffractors located at $\mathbf{x}_A$ and $\mathbf{x}_B$ is set to -1, for the scatterer at $\mathbf{x}_C$ it is set to -2.

Figure 17. Pseudo-physical events (solid line) constructed using $G_S G_S G_S^*$ only and the geometry shown in Fig. 16 containing three diffractors. The dashed line represents the true scattered Green's function. All first-order scattering events (primaries) are constructed with the correct traveltime and waveform. According to eq. (13) the primaries around 0.2 and 0.3 s have exactly the amplitude of the true events, since the imaginary part of the scattering amplitude of the corresponding scatterers ($\Im(A_A)$ and $\Im(A_B)$, respectively) equals -1. Analogously, the primary at 0.6 s is constructed with twice the correct amplitude, since $\Im(A_C) = -2$. Moreover, good estimates of higher-order scattering events have been constructed, for example, between 0.4 and 0.6 s and around 0.8 s. Note, however, that they appear to be shifted in phase. The small amplitude events before 0.15 s are non-physical.

imaging condition can be derived from SRI even if the boundaries are only partially available on top of the scattering medium. Indeed the suppression of the two non-physical events when using partial boundaries can be seen as a positive advantage of using incomplete boundaries, since that non-physical energy will not disturb the image.

As the interferometric approach does not make use of the Born approximation it is in principle able to account for non-linearities associated with multiple scatterers, which are currently not considered by standard migration schemes. When an initial estimate of the scattered wavefield is included in the reference wavefield G_0 it also becomes possible to use additional interferometric terms for non-linear imaging, and some work has already been done in this area (Fleury & Vasconcelos 2012; Ravasi & Curtis 2013; Vasconcelos 2013). The question of how our specific results generalize to the case of a multiply scattering medium, and how this could be used to enhance resolution in seismic images, will be addressed in future research. An example for pseudo-physical energy constructed in a multiple scattering case is provided in Fig. 17. A full boundary has been used (Fig. 16) to highlight the effect of the scattering amplitude on the amplitude of the constructed events. For first-order scattering the analysis provided for a single scatterer applies just as well in the multiple-scattering case: the amplitude of the constructed event is proportional to the imaginary part of the scattering amplitude of the corresponding scatterer. Note that the scatterers have different scattering amplitudes, which results in different amplitudes of the primary events on the constructed trace. In principle, scattering events of any order are constructed using $G_S G_S G_S^*$ only. For example, a secondary event can be seen at around 0.7 s. For a kinematic analysis of higher order scattering see Meles & Curtis (2013). How the amplitude (and phase) is affected by the scattering amplitudes of the individual diffractors has to be clarified in future research. Moreover, non-physical events are introduced from the correlation of cross-terms (e.g. at 0.2 s). Note that those may superimpose pseudo-physical arrivals and affect their amplitudes and waveforms. Nevertheless, this example shows that the single-scattering analysis presented herein is useful and applicable, at least in relatively simple multiple-scattering scenarios.

CONCLUSIONS

Using synthetic acoustic scattered waves we have illustrated the ability of SRI to provide information about scatterers embedded in a smooth background medium using a limited geometry of source and receiver boundaries representing linear arrays used in industrial geophysics. By separating the wavefield into a background component and a scattered wave component and analysing individual cross-terms of the interferometric equation using the method of stationary phase, we determine the origin of both physical and non-physical energy in the resulting Green's function estimates. We identify a new category of non-physical energy, referred to as *pseudo*-physical energy, which can be used to estimate physical energy directly.

We show that the scattered wave is constructed by only one term of the equation, referred to as $G_0 G_0 G_S^*$, which is directly linked to the imaging condition used in standard seismic migration schemes. We showed that for this term the partial boundary may be a positive advantage as this suppresses non-physical energy in resulting images. The term $G_S G_S G_S^*$ provides a pseudo-physical event, which is naturally non-physical but can be used as an estimate of the causal scattered wave. For the first time a complete mathematical derivation for the generation of pseudo-physical energy is provided. Two other terms contain stationary non-physical energy that is not cancelled out when using incomplete boundaries; however, this energy was shown to provide novel information about the location of scatterers. Non-stationary, non-physical energy associated with the abrupt truncation of the boundaries and the monopole approximation can be reduced by using a spatial taper, the use of dipole sources, or the elimination of the direct wave component between the boundaries, $G_0(\mathbf{x}', \mathbf{x})$, prior to the cross-correlation of wavefields. Considering source and receiver coverage along the boundaries, our studies reveal four terms that permit deviations from theoretical sampling requirements while still providing a reliable estimate of stationary energy, and fortunately for practical applications, these include the two terms $G_0 G_0 G_S^*$ and $G_S G_S G_S^*$ that construct the (pseudo-)physical scattered waves.

ACKNOWLEDGEMENTS

REFERENCES

Berkovitch, A., Belfer, I., Hassin, Y. & Landa, E., 2009. Diffraction imaging by multifocusing, *Geophysics,* **74,** WCA75–WCA81.

Born, M. & Wolf, E., 1999. *Principles of Optics: Electromagnetic Theory of Propagation, Interference and Diffraction of Light,* Cambridge Univ. Press.

Campillo, M. & Paul, A., 2003. Long-range correlations from the diffuse seismic coda, *Science,* **299,** 547–549.

Claerbout, J., 1985. *Imaging the Earth's Interior,* Blackwell Scientific Publications.

Curtis, A. & Halliday, D., 2010. Source-receiver wavefield interferometry, *Phys. Rev. E,* **81,** 046601,1–046601,10.

Curtis, A., Gerstoft, P., Sato, H., Snieder, R. & Wapenaar, K., 2006. Seismic interferometry—turning noise into signal, *Leading Edge,* **25,** 1082–1092.

Curtis, A., Nicolson, H., Halliday, D., Trampert, J. & Baptie, B., 2009. Virtual seismometers in the subsurface of the earth from seismic interferometry, *Nat. Geosci.,* **2,** 700–704.

Curtis, A., Behr, Y., Entwistle, E., Galetti, E., Townend, J. & Bannister, S., 2012. The benefit of hindsight in observational science: retrospective seismological observations, *Earth planet. Sci. Lett.,* **345,** 212–220.

Derode, A., Larose, E., Tanter, M., De Rosny, J., Tourin, A., Campillo, M. & Fink, M., 2003. Recovering the Green's function from field-field correlations in an open scattering medium, *J. acoust. Soc. Am.,* **113,** 2973–2976.

Duguid, C., Halliday, D. & Curtis, A., 2011. Source-receiver interferometry for seismic wavefield construction and ground-roll removal, *Leading Edge,* **30**(8), 838–843.

Faccipieri, J.H., Rueda Serrano, D., Gelius, L.-J. & Tygel, M., 2013. Recovering diffractions in CRS stacked sections, *First Break,* **31,** 65–69.

Fleury, C. & Vasconcelos, I., 2012. Imaging condition for nonlinear scattering-based imaging: estimate of power loss in scattering, *Geophysics,* **77,** S1–S18.

Foldy, L., 1945. The multiple scattering of waves. I. General theory of isotropic scattering by randomly distributed scatterers, *Phys. Rev.,* **67,** 107–119.

Galetti, E. & Curtis, A., 2012. Generalised receiver functions and seismic interferometry, *Tectonophysics,* **532–535,** 1–26.

Galetti, E., Halliday, D. & Curtis, A., 2013. A simple and exact acoustic wavefield modelling code for data processing, imaging and interferometry applications, *Geophysics,* **78**(6), F17–F27.

Groenenboom, J. & Snieder, R., 1995. Attenuation, dispersion, and anisotropy by multiple scattering of transmitted waves through distributions of scatterers, *J. acoust. Soc. Am.,* **98,** 3482–3492.

Halliday, D. & Curtis, A., 2009. Seismic interferometry of scattered surface waves in attenuative media, *Geophys. J. Int.,* **178,** 419–446.

Halliday, D. & Curtis, A., 2010. An interferometric theory of source-receiver scattering and imaging, *Geophysics,* **75,** SA95–SA103.

Harmankaya, U., Kaslilar, A., Thorbecke, J., Wapenaar, K. & Draganov, D., 2013. Locating near-surface scatterers using non-physical scattered waves resulting from seismic interferometry, *J. appl. Geophys.,* **91,** 66–81.

Hong, T. & Menke, W., 2006. Tomographic investigation of the wear along the San Jacinto fault, southern California, *Phys. Earth planet. Inter.,* **155,** 236–248.

Khaidukov, V., Lande, E. & Moser, T., 2004. Diffraction imaging by focusing-defocusing: an outlook on seismic superresolution, *Geophysics,* **69,** 1478–1490.

King, S. & Curtis, A., 2011. Velocity analysis using both reflections and refractions from seismic interferometry, *Geophysics,* **76,** SA83–SA96.

King, S. & Curtis, A., 2012. Suppressing non-physical reflections in Green's function estimates using source-receiver interferometry, *Geophysics,* **77,** Q15–Q25.

King, S., Curtis, A. & Poole, T., 2011. Interferometric velocity analysis using physical and non-physical energy, *Geophysics,* **76,** SA35–SA49.

Lobkis, O. & Weaver, R., 2001. On the emergence of the Green's function in the correlations of a diffuse field, *J. acoust. Soc. Am.,* **110,** 3011–3017.

Mehta, K., Snieder, R., Calvert, R. & Sheiman, J., 2008. Acquisition geometry requirements for generating virtual-source data, *Leading Edge,* **27,** 620–629.

Meles, G.A. & Curtis, A., 2013. Physical and non-physical energy in scattered wave interferometry, *J. acoust. Soc. Am.,* **133,** 3790–3801.

Mikesell, D., van Wijk, K., Calvert, A. & Haney, M., 2009. The virtual refraction: useful spurious energy in seismic interferometry, *Geophysics,* **74,** A13–A17.

Miller, D., Oristaglio, M. & Beylkin, G., 1987. A new slant on seismic imaging: classical migration and integral geometry, *Geophysics,* **52,** 943–964.

Oristaglio, M., 1989. An inverse scattering formula that uses all the data, *Inverse Problems,* **5,** 197–1105.

Poliannikov, O.V., 2011. Retrieving reflections by source-receiver wavefield interferometry, *Geophysics,* **76,** SA1–SA8.

Poliannikov, O.V., Rondenay, S. & Chen, L., 2012. Interferometric imaging of the underside of a subducting crust, *Geophys. J. Int.,* **189,** 681–690.

Pratt, G., 1999. Seismic waveform inversion in the frequency domain. Part 1: theory and verification in a physical scale model, *Geophysics,* **64,** 888–901.

Ravasi, M. & Curtis, A., 2013. Non-linear scattering based imaging in elastic media: theory, theorems and imaging conditions, *Geophysics,* **78**(3), S137–S155.

Schuster, G.T., 2009. *Seismic Interferometry,* Cambridge Univ. Press.

Snieder, R., 1999. Imaging and averaging in complex media, in *Diffuse Waves in Complex Media*, Vol. 531 of NATO Science Series - Series C: Mathematical and Physical Sciences, pp. 405–454, Kluwer.

Snieder, R., 2004a. *A Guided Tour of Mathematical Methods for the Physical Sciences,* Cambridge Univ. Press.

Snieder, R., 2004b. Extracting the Green's function from the correlation of coda waves: a derivation based on stationary phase, *Phys. Rev. E,* **69,** 046610,1–046610,8.

Snieder, R. & Fleury, C., 2010. Cancellation of spurious arrivals in Green's function retrieval of multiple scattered waves, *J. acoust. Soc. Am.,* **128,** 1598–1605.

Snieder, R., Wapenaar, K. & Larner, K., 2006. Spurious multiples in seismic interferometry of primaries, *Geophysics,* **71,** SI111–SI124.

Snieder, R., van Wijk, K., Haney, M. & Calvert, R., 2008. Cancellation of spurious arrivals in Green's function extraction and the generalized optical theorem, *Phys. Rev. E,* **78,** 036606,1–036606,8.

Van Manen, D., Curtis, A. & Robertsson, J., 2005. Modeling of wave propagation in inhomogeneous media, *Phys. Rev. Lett.,* **94,** 164301,1–164301,4.

Van Manen, D., Curtis, A. & Robertsson, J., 2006. Interferometric modeling of wave propagation in homogeneous elastic media using time reversal and reciprocity, *Geophysics,* **71,** SI47–SI60.

Vasconcelos, I., 2013. Source-receiver, reverse-time imaging of dual-source, vector-acoustic seismic data, *Geophysics,* **78,** WA123–WA145.

Vasconcelos, I., Snieder, R. & Douma, H., 2009. Representation theorems and Green's function retrieval for scattering in acoustic media, *Phys. Rev. E,* **80,** 036605–036618.

Vasconcelos, I., Sava, P. & Douma, H., 2010. Nonlinear extended images via image-domain interferometry, *Geophysics,* **75,** SA105–SA115.

Wapenaar, K., 2004. Retrieving the elastodynamic Green's function of an arbitrary inhomogeneous medium by cross correlation, *Phys. Rev. Lett.,* **93,** 254301,1–254301,4.

Wapenaar, K. & Fokkema, J., 2006. Green's function representations for seismic interferometry, *Geophysics,* **71,** SI33–SI46.

Wapenaar, K., Fokkema, J. & Snieder, R., 2005. Retrieving the Green's function in an open system by cross correlation: a comparison of approaches, *J. acoust. Soc. Am.,* **118,** 2783–2786.

Wapenaar, K., Draganov, D., Snieder, R., Campman, X. & Verdel, A., 2010a. Tutorial on seismic interferometry. Part 1—basic principles and applications, *Geophysics,* **75,** 75A195–75A209.

Wapenaar, K., Slob, E., Snieder, R. & Curtis, A., 2010b. Tutorial on seismic interferometry. Part 2—underlying theory and new advances, *Geophysics,* **75,** 75A211–75A227.

Wapenaar, K., Slob, E. & Snieder, R., 2010c. On seismic interferometry, the generalized optical theorem, and the scattering matrix of a point scatterer, *Geophysics,* **75,** SA27–SA35.

Yilmaz, Ö., 2001. *Seismic Data Analysis: Processing, Inversion, and Interpretation of Seismic Data,* 2nd edn, SEG Books.

APPENDIX A: THE METHOD OF STATIONARY PHASE

The method of stationary phase is a procedure that provides an approximate evaluation of integrals of the form

$$I = \int_{-\infty}^{\infty} F(x)\, e^{[-j\varphi(x)]}\, dx, \tag{A1}$$

where the function $F(x)$ varies slowly with x compared to the phase term $\varphi(x)$ (Snieder 2004; Schuster 2009). As the exponential term is rapidly oscillating over most of the range of integration it can be shown that its contribution to the integral will be zero apart from the so-called points of stationary phase x_s, where $\varphi'(x_s) = 0$. The Taylor series expansion for $\varphi(x)$ around the stationary point x_s up to second order is given by

$$\varphi(x) \approx \varphi(x_s) + \varphi''(x_s)\frac{(x - x_s)^2}{2}. \tag{A2}$$

Note that because $\varphi'(x_s) = 0$ it is omitted in eq. (A2). Because the function $F(x)$ is slowly varying with x, close to each stationary phase point it can be replaced by its value at the stationary point, $F(x_s)$, and taken outside of the integral. Substituting the Taylor expansion into eq. (A2) this yields

$$I \approx F(x_s)\, e^{-j\varphi(x_s)} \int_{-\infty}^{\infty} e^{-j\varphi''(x_s)\frac{(x-x_s)^2}{2}}\, dx$$

$$\approx F(x_s)\, e^{-j\varphi(x_s)} \sqrt{\frac{2\pi}{j\varphi''(x_s)}}. \tag{A3}$$

There will be one such approximation for each stationary point x_s, and the set of such approximations may be summed. eq. (A3) shows that the main contribution to the integral in eq. (A1) comes from the points x_s where the phase is stationary, in short, the *stationary points*.

APPENDIX B: PSEUDO-PHYSICAL ENERGY

In this study we show that the term $G_S G_S G_S^*$ constructs an event that arrives at the traveltime of the causal scattered wave $G_S(\mathbf{x}_2, \mathbf{x}_1)$ and—after normalization of amplitudes—perfectly matches the waveform of the causal part of the modelled scattered Green's function (e.g. Figs 15c and d). This appendix provides an alternative mathematical development that explains why, despite its physical appearance, the event constructed from $G_S G_S G_S^*$ is in fact non-physical, and moreover why it can still be used as an estimate of a physical event.
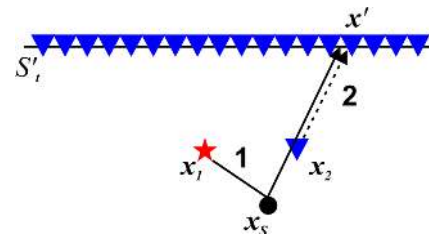
Figure B1. Sketch of ray paths constructing $G_S(\mathbf{x}_2, \mathbf{x}_1)$ from intersource interferometry according to eq. (B1). Ray paths shown are 1: $G_S(\mathbf{x}', \mathbf{x}_1)$ and 2: $G_0^*(\mathbf{x}', \mathbf{x}_2)$. Symbol key as in Fig. 2. The dashed line indicates complex conjugation, that is, solid and dashed lines that run parallel cancel each other in phase. Since $\mathbf{x}_2$ is in fact a receiver location, $G_0^*(\mathbf{x}', \mathbf{x}_2)$ needs to be constructed from interreceiver interferometry (see Fig. B2 or B3), which turns the receiver at $\mathbf{x}_2$ into a virtual source.
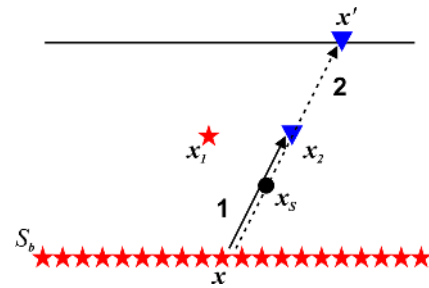
Figure B2. Sketch of ray paths constructing $G_0^*(\mathbf{x}', \mathbf{x}_2)$ from interreceiver interferometry according to eq. (B2). Ray paths shown are (1) $G_0(\mathbf{x}_2, \mathbf{x})$ and (2) $G_0^*(\mathbf{x}, \mathbf{x}')$. Symbol key as in Fig. B1.

The derivation is based on representations for scattered fields introduced by Vasconcelos *et al.* (2009), for performing intersource and thereafter interreceiver interferometry. Halliday & Curtis (2009) and Vasconcelos *et al.* (2009) show that in intersource interferometry the causal scattered wave is provided by stationary point contributions from the top boundary of receivers (S_t') according to

$$G_S(\mathbf{x}_2, \mathbf{x}_1) = \frac{2}{\rho c} \int_{S_t'} G_S(\mathbf{x}', \mathbf{x}_1)\, G_0^*(\mathbf{x}', \mathbf{x}_2)\, dS_t'. \tag{B1}$$

A sketch of the corresponding ray paths is given in Fig. B1. We now assume that, as before, $\mathbf{x}_2$ is a receiver location; hence, $G_0^*(\mathbf{x}', \mathbf{x}_2)$ is not available and needs to be constructed from interreceiver interferometry using

$$G_0^*(\mathbf{x}', \mathbf{x}_2) = \frac{2}{\rho c} \int_{S_b} G_0(\mathbf{x}_2, \mathbf{x})\, G_0^*(\mathbf{x}', \mathbf{x})\, dS_b, \tag{B2}$$

where S_b denotes a bottom boundary of sources, as shown in Fig. B2. However, if S_b is not available because the source locations are restricted to the surface, $G_0^*(\mathbf{x}', \mathbf{x}_2)$ cannot be constructed and $G_S(\mathbf{x}_2, \mathbf{x}_1)$ in eq. (B1) is not retrieved.

Note that when substituting eq. (B2) into eq. (B1) we obtain a double surface integral corresponding to the term $G_S G_0 G_0^*$. According to Fig. 3 and Table 1 this term accounts for the construction of the causal scattered wave; however, as the associated stationary point pair ($\mathbf{x} = \mathbf{d}$, $\mathbf{x}' = \mathbf{c}$ in Fig. 3) is not included in the surface boundaries this wave is not retrieved in our examples (Fig. 9h). In this case we can still construct an event that *looks like* the required direct wave by cross-correlating scattered fields according to

$$\hat{G}_0^*(\mathbf{x}', \mathbf{x}_2) = \frac{2}{\rho c} \int_{S_t} G_S(\mathbf{x}_2, \mathbf{x})\, G_S^*(\mathbf{x}', \mathbf{x})\, dS_t. \tag{B3}$$
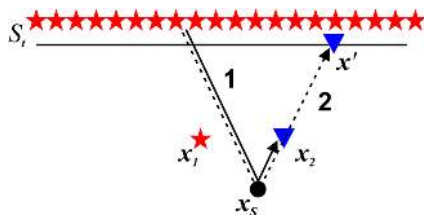
Figure B3. Sketch of ray paths constructing $\hat{G}_0^*\left(\mathbf{x}', \mathbf{x}_2\right)$ from interreceiver interferometry according to eq. (B3). Ray paths shown are (1) $G_S\left(\mathbf{x}_2, \mathbf{x}\right)$ and (2) $G_S^*\left(\mathbf{x}', \mathbf{x}\right)$. Symbol key as in Fig. B1.

Fig. B3 shows a sketch of the corresponding ray paths. However, the Green's functions on the right-hand side of eq. (B3) interact with the scatterer and hence carry information about the scattering matrix. Therefore the left-hand side of eq. (B3) is not equal to a direct wave since it must also contain information about the scatterer. Snieder *et al.* (2006) apply a similar argument for waves reflected at an interface: the apparent direct wave constructed from cross-correlation of reflected wavefields contains a factor proportional to the reflection coefficient. Inserting eq. (B3) into eq. (B1) gives the double surface integral representing the term $G_S G_S G_S^*$.

SUPPORTING INFORMATION

Additional Supporting Information may be found in the online version of this article:

Figure C1. Interferometric result of the full integral GGG^* of eq. (8) (solid line) compared to the true Green's function between $\mathbf{x}_1$ and $\mathbf{x}_2$ (dashed line) for different parameter constellations (see Table 2). Maximum Amplitudes have been normalized to one.

Figure C2. Example set of ray paths used in $G_0 G_0 G_S^*$, symbol key as in Fig. 2. The dashed line represents the ray of the complex conjugated term. Faded symbols are used to make ray paths visible. Rays shown are 1: $G_0(\mathbf{x}', \mathbf{x}_1)$, 2: $G_0(\mathbf{x}_2, \mathbf{x})$, 3: $G_S^*(\mathbf{x}', \mathbf{x})$.

Figure C3. Interferometric result of the cross-term $G_0 G_0 G_S^*$ in eq. (8) (solid line) compared to the true Green's function between $\mathbf{x}_1$ and $\mathbf{x}_2$ (dashed line) for different parameter constellations (see Table 2). Traces have amplitudes that are normalized relative to case (a). Number labels are referred to in the text.

Figure C4. Example set of ray paths used in $G_S G_S G_S^*$, symbol key as in Fig. C2. Rays shown are 1: $G_S(\mathbf{x}', \mathbf{x}_1)$, 2: $G_S(\mathbf{x}_2, \mathbf{x})$, 3: $G_S^*(\mathbf{x}', \mathbf{x})$.

Figure C5. Interferometric result of the cross-term $G_S G_S G_S^*$ in eq. (8) (solid line) compared to the true Green's function between $\mathbf{x}_1$ and $\mathbf{x}_2$ (dashed line) for different parameter constellations (see Table 2). Traces have amplitudes that are normalized relative to case (a).

Figure C6. Example set of ray paths used in $G_0 G_S G_S^*$, symbol key as in Fig. C2. Rays shown are 1: $G_0(\mathbf{x}', \mathbf{x}_1)$, 2: $G_S(\mathbf{x}_2, \mathbf{x})$, 3: $G_S^*(\mathbf{x}', \mathbf{x})$.

Figure C7. $G_0 G_S G_S^*$ for different apertures (length *ls*) of both source (*ls*) and receiver (*ls*–100) boundary showing a stationary

(–0.05 s) and a non-stationary (between 0.1 and 0.2 s) non-physical arrival.

Figure C8. Interferometric result of the cross-term $G_0 G_S G_S^*$ in eq. (8) (solid line) compared to the true Green's function between $\mathbf{x}_1$ and $\mathbf{x}_2$ (dashed line) for different parameter constellations (see Table 2). Traces have amplitudes that are normalized relative to case (a).

Figure C9. Example set of ray paths used in $G_S G_0 G_S^*$, symbol key as in Fig. C2. Rays shown are 1: $G_S(\mathbf{x}', \mathbf{x}_1)$, 2: $G_0(\mathbf{x}_2, \mathbf{x})$, 3: $G_S^*(\mathbf{x}', \mathbf{x})$.

Figure C10. Interferometric result of the cross-term $G_S G_0 G_S^*$ in eq. (8) (solid line) compared to the true Green's function between $\mathbf{x}_1$ and $\mathbf{x}_2$ (dashed line) for different parameter constellations (see Table 2). Traces have amplitudes that are normalized relative to case (a).

Figure C11. Example set of ray paths used in $G_0 G_0 G_S^*$, symbol key as in Fig. C2. Rays shown are 1: $G_0(\mathbf{x}', \mathbf{x}_1)$, 2: $G_0(\mathbf{x}_2, \mathbf{x})$, 3: $G_0^*(\mathbf{x}', \mathbf{x})$.

Figure C12. $G_0 G_0 G_0^*$ for different depths $\mathbf{d}_2$ showing the moveout of non-stationary events.

Figure C13. Interferometric result of the cross-term $G_0 G_0 G_0^*$ in eq. (8) (solid line) compared to the true Green's function between $\mathbf{x}_1$ and $\mathbf{x}_2$ (dashed line) for different parameter constellations (see Table 2). Traces have amplitudes that are normalized relative to case (a).

Figure C14. Example set of ray paths used in $G_S G_S G_0^*$, symbol key as in Fig. C2. Rays shown are 1: $G_S(\mathbf{x}', \mathbf{x}_1)$, 2: $G_S(\mathbf{x}_2, \mathbf{x})$, 3: $G_0^*(\mathbf{x}', \mathbf{x})$.

Figure C15. Interferometric result of the cross-term $G_S G_S G_0^*$ in eq. (8) (solid line) compared to the true Green's function between $\mathbf{x}_1$ and $\mathbf{x}_2$ (dashed line) for different parameter constellations (see Table 2). Traces have amplitudes that are normalized relative to case (a).

Figure C16. Example set of ray paths used in $G_0 G_S G_0^*$, symbol key as in Fig. C2. Rays shown are 1: $G_0(\mathbf{x}', \mathbf{x}_1)$, 2: $G_S(\mathbf{x}_2, \mathbf{x})$, 3: $G_0^*(\mathbf{x}', \mathbf{x})$.

Figure C17. Interferometric result of the cross-term $G_0 G_S G_0^*$ in eq. (8) (solid line) compared to the true Green's function between $\mathbf{x}_1$ and $\mathbf{x}_2$ (dashed line) for different parameter constellations (see Table 2). Traces have amplitudes that are normalized relative to case (a).

Figure C18. Example set of ray paths used in $G_S G_0 G_0^*$, symbol key as in Fig. C2. Rays shown are 1: $G_S(\mathbf{x}', \mathbf{x}_1)$, 2: $G_0(\mathbf{x}_2, \mathbf{x})$, 3: $G_0^*(\mathbf{x}', \mathbf{x})$.

Figure C19. Interferometric result of the cross-term $G_S G_0 G_0^*$ in eq. (8) (solid line) compared to the true Green's function between $\mathbf{x}_1$ and $\mathbf{x}_2$ (dashed line) for different parameter constellations (see Table 2). Traces have amplitudes that are normalized relative to case (a). Inset in (d) shows detail (http://gji.oxfordjournals.org/lookup/suppl/doi:10.1093/gji/ggt435/-/DC1).

Please note: Oxford University Press are not responsible for the content or functionality of any supporting materials supplied by the authors. Any queries (other than missing material) should be directed to the corresponding author for the article.